nature metabolism

ARTICLES

https://doi.org/10.1038/s42255-020-00278-3

Check for updates

A large-scale genome–lipid association map guides lipid identification

Vanessa Linke[1], Katherine A. Overmyer[2,3], Ian J. Miller[3], Dain R. Brademan[1], Paul D. Hutchins[1], Edna A. Trujillo[1], Thiru R. Reddy[2,3], Jason D. Russell[2], Emily M. Cushing[4], Kathryn L. Schueler[4], Donald S. Stapleton[4], Mary E. Rabaglia[4], Mark P. Keller[4], Daniel M. Gatti[5], Gregory R. Keele[5], Duy Pham[5], Karl W. Broman[6], Gary A. Churchill[5], Alan D. Attie[4] and Joshua J. Coon[1,3]✉

Despite the crucial roles of lipids in metabolism, we are still at the early stages of comprehensively annotating lipid species and their genetic basis. Mass spectrometry–based discovery lipidomics offers the potential to globally survey lipids and their relative abundances in various biological samples. To discover the genetics of lipid features obtained through high-resolution liquid chromatography–tandem mass spectrometry, we analysed liver and plasma from 384 diversity outbred mice, and quantified 3,283 molecular features. These features were mapped to 5,622 lipid quantitative trait loci and compiled into a public web resource termed LipidGenie. The data are cross-referenced to the human genome and offer a bridge between genetic associations in humans and mice. Harnessing this resource, we used genome–lipid association data as an additional aid to identify a number of lipids, for example gangliosides through their association with *B4galnt1*, and found evidence for a group of sex-specific phosphatidylcholines through their shared locus. Finally, LipidGenie's ability to query either mass or gene-centric terms suggests acyl-chain-specific functions for proteins of the ABHD family.

Beyond their roles in energy storage and membrane structure, lipids are central actors in myriad metabolic functions and molecular signalling[1,2]. As our understanding of these diverse lipid functions grows, so too does our appreciation for the complexity of the lipidome of mammalian systems[3]. Mass spectrometry (MS) has emerged as the central tool to dissect and quantify the myriad of lipid species beyond traditional clinical measures[4–6]. Specifically, using liquid chromatography (LC) coupled with high-resolution tandem MS (LC–MS/MS), over 1,000 unique lipid features from a complex mixture can be quantified in under an hour (ref. [7]). A chromatographic feature in this context is defined by a unique combination of mass and retention time. From these features, hundreds of individual lipids are routinely identified; however, most of the features remain unannotated[8,9]. The result is that more often than not, most MS data are not leveraged[8,10,11].

One strategy for lipid feature identification is to group compounds likely to be related. For example, members of a lipid class often (1) appear within a defined chromatographic retention time, (2) occupy a characteristic mass range and (3) exhibit similar dissociation patterns when subjected to fragmentation[12]. Most efforts to improve lipid identification rates exploit one or all of these steps[3,13–15], including our laboratory's recent description of a software suite that constructs tailored MS/MS libraries for automated lipid spectral identification[16,17]. Others have sought to build on this information by adding external complementary data, such as measurement of collisional cross section[10], or labile hydrogen counting[18]. All of these methods show great promise but share the common theme that they incorporate lipid chemical properties into their identification inference.

In the field of shotgun proteomics, genome sequence data are used to identify experimental peptide tandem mass spectra. Given the success of this field we wondered whether genomic information could be leveraged similarly in the field of lipidomics. Unfortunately, it is not possible to directly predict lipid identities from genomic data; however, shared genetic regulation among lipids could provide key information to facilitate identification. For example, a recent large-scale multi-omic study of a knock-out yeast library demonstrated dramatic regulation of the lipidome[19], nuclear magnetic resonance (NMR)-based untargeted metabolomics identified disease-associated metabolites and genomic regions via quantitative trait loci (QTL) mapping[20,21] and, in humans, data from genome-wide association studies (GWAS) were used to assist in small molecule identifications from both MS and NMR data[22–25]. We thus aimed to create a global genome–lipid association map that would offer genetic location as a fourth, orthogonal dimension of data to assist in lipid feature identification.

To construct a global genome–lipid association map we measured plasma and liver lipids from a mouse population using LC–MS/MS and performed QTL mapping[26–28]. This study is carried out using diversity outbred (DO) mice, a multiparent population (MPP)[29] derived from eight highly diverse founder strains (FSs) (Fig. 1a)[24–26]. A key advantage of the MPP is that we can identify the additive genetic effects contributed by each FS at a quantitative trait locus. Unlike standard biparental crosses where the founder haplotype effects are either increasing or decreasing, the haplotype effects in a MPP are complex and enable us to distinguish chance colocalization from pleiotropic effects. In addition, we can compare founder haplotype effects across different studies using DO mice to identify shared effects on traits that were not directly measured in only one group of DO mice. Specifically, we were able to use liver gene expression from a previously published study to propose

[1]Department of Chemistry, University of Wisconsin–Madison, Madison, WI, USA. [2]Morgridge Institute for Research, Madison, WI, USA. [3]Department of Biomolecular Chemistry, University of Wisconsin–Madison, Madison, WI, USA. [4]Department of Biochemistry, University of Wisconsin–Madison, Madison, WI, USA. [5]The Jackson Laboratory, Bar Harbor, ME, USA. [6]Department of Biostatistics and Medical Informatics, University of Wisconsin–Madison, Madison, WI, USA. ✉e-mail: jcoon@chem.wisc.edu

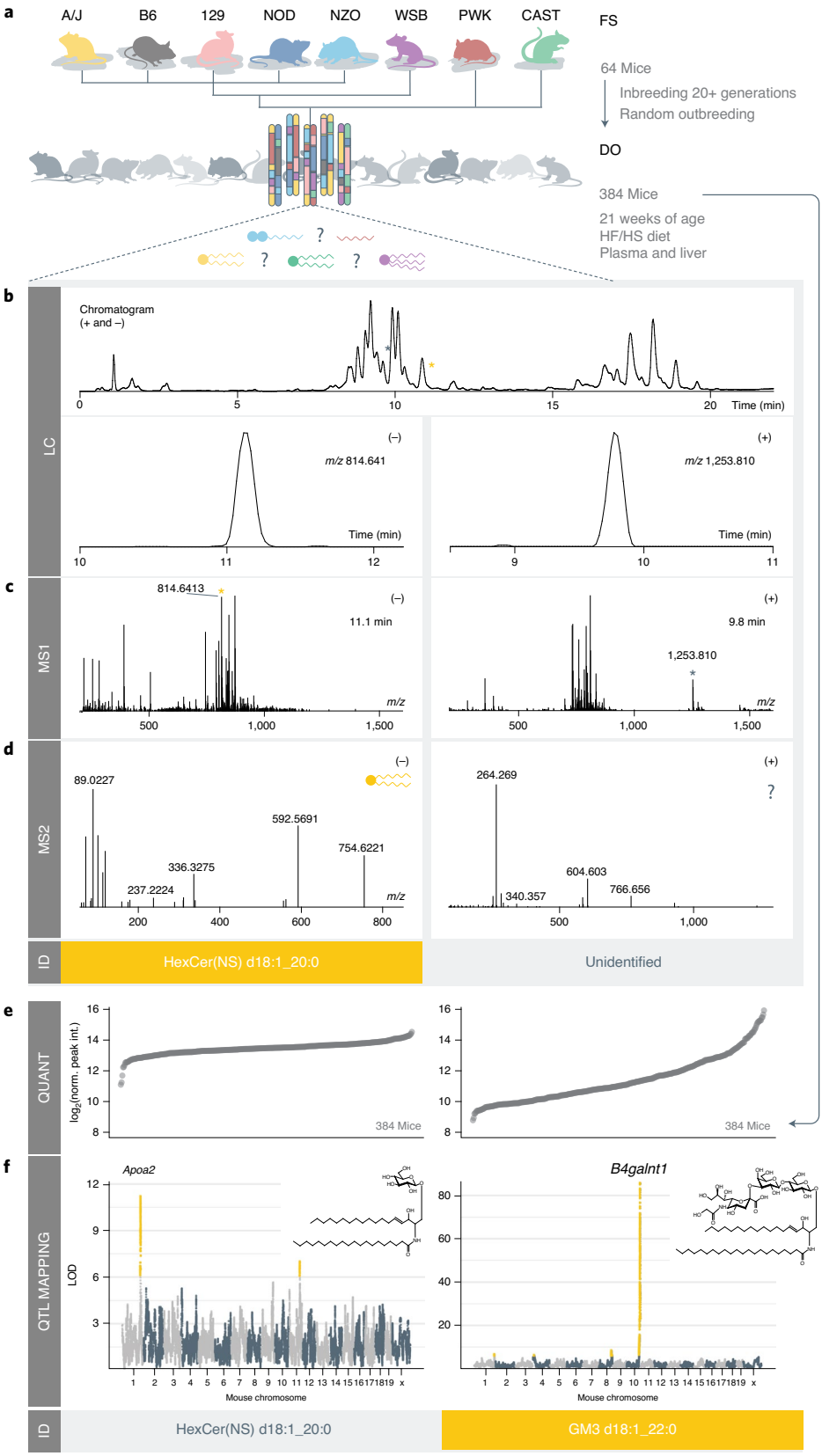

Fig. 1 | LC–MS/MS lipidomics and QTL mapping as ways to lipid identification. a, A modified MTBE lipid extraction[92] was performed on plasma and liver from 64 FS and 384 DO mice. **b**–**d**, Lipid extracts were analysed by LC–MS/MS. Identifications were obtained through LipiDex[16] on the basis of retention time window (**b**), exact mass (**c**), retention time window and tandem mass fragmentation (**d**). **e**, Quantitative values over large dynamic ranges for both identified and unidentified features were obtained. **f**, All lipidomic features (identified and unidentified) were then mapped onto the mouse genome via QTL mapping, revealing genomic position and FS allele effect pattern as results for each QTL. This additional information enabled identification of otherwise unidentified features. RT, retention time; HF/HS, high-fat/high-sucrose.

candidate genes for the lipid features in this study[30]. Further, each of the eight inbred DO founder mouse strains (129, A/J, B6, CAST, non-obese diabetic (NOD), NZO, PWK, WSB) contributes to generate distinct allele effect patterns at each locus, thus providing an additional criterion for gene identification[31]. Finally, careful control of external sources of variation such as diet and environmental conditions, allows the extraordinary phenotypic diversity of the DO[32] to be directly attributed to genetic diversity. The DO population has already been used extensively to map clinical traits[33], transcripts[32], proteins[34], gut microbiota and bile acids[35] providing a wealth of existing data to integrate with global genome–lipid associations.

Here we describe discovery lipidomics analysis on a cohort of DO mice. In doing so, we use QTL position as an independent piece of information to guide lipid identification and apply it to define unidentified mass spectral features. We demonstrate the use of genome–lipid associations to assign identification or function in independent studies through a web-based resource, LipidGenie (http://lipidgenie.com/).

Results

QTL mapping connects lipids to their genetic regulators. To explore how global association of MS data to genomic coordinates could assist in lipid identification, we collected whole lipidome profiles of plasma and liver tissue from 64 FS and 384 DO mice by using high-resolution LC–MS/MS (Fig. 1a). Altogether, we performed 894 LC–MS/MS discovery lipidomics experiments from which we extracted approximately 4,500,000 tandem mass spectra (Fig. 1d). From the full scan MS data (Fig. 1c), we detected and quantified 19,636 molecular features: 12,429 in plasma and 7,207 in liver (Fig. 1b). Next, we applied the LipiDex algorithm[16] to (1) match the tandem mass spectra to their respective features, (2) eliminate features derived from adduction, dimerization, in-source fragmentation and so on, and (3) to assign molecular identities when possible (Fig. 1d). From the 3,283 distinct molecular features that remained, we identified 594 lipids (from 1,721 features) in plasma and 584 lipids (from 1,562 features) in liver (see Lipidomics data analysis in the Methods for details). This discovery approach allows for broad, untargeted lipidome coverage. However, we note that some lipid classes, including PS, LysoPS, PA, LysoPA, LysoPG and cholesterol, are either partially or wholly, missed by the current method. For instance, reversed-phase–electrospray ionization (ESI)–tandem MS poorly retains phosphatidic acid (PA) and phosphatidylserine (PS) species. Further, cholesterols and other sterols have poor ESI efficiencies[5,9,36,37]. Extended Data Fig. 2a,b and Table 1 provide an overview of the identified lipids that span roughly 30 lipid subclasses from five of the main classes: fatty acyls, glycerolipids, phospholipids, sphingolipids and sterol lipids[38]. For ~70% of these identifications, we find MS/MS evidence to detail fatty acid composition; otherwise, we report sum composition.

Extended Data Fig. 1a,b presents a bird's-eye view of these plasma and liver lipidomes. Here each distinct molecular feature is plotted as a function of its *m/z* and chromatographic retention time. Identified lipids are coloured by class; we note members of individual lipid classes group well, adding confidence to their identification. Triglycerides[39], for example, as hydrophobic lipids with three fatty acids can be found at high *m/z* and late chromatographic retention. From this perspective, we observe that the unidentified molecular features, two-thirds of all detected species, are either clustered around identified lipid classes or exist on *m/z* and retention islands. We conclude that these data can be further interrogated to (1) expand existing lipid class coverage and (2) reveal the presence of additional lipid classes.

Next, we extracted quantitative information from all detected molecular features across all 384 animals, creating a molecular trait for each feature. Figure 1e displays the quantitative values of two examples of individual molecular traits from plasma, one identified as a sphingolipid and one unidentified. Plasma HexCer[NS] d18:1_20:0 has a relative abundance dynamic range of ~15-fold across all 384 animals. For comparison, we plot the abundance of a molecular feature with a mass of 1,252.8028 Da. Here we see an even greater dynamic range of ~75-fold, however, the feature was unidentified using our traditional data processing. Correlation to a candidate gene region ultimately led to the identification of the feature. To correlate these MS-derived lipid quantitative phenotypes (vide supra) with genomic variation we performed quantitative trait locus (QTL) mapping using R/qtl2 (ref. [27]).

Figure 2a displays a hierarchically clustered heatmap of these quantitative results for all measured molecular traits (1,721 and 1,562 for plasma and liver, respectively) across all 384 animals. Notably, we observe considerable clustering by lipid class, even across tissue type (*y* axis). We detected 3,348 plasma lipid QTL for 1,405 of the 1,721 (81.6%) traits (logarithm of odds (LOD) score > 6). 1,351 of these were from identified lipids, while 1,997 were from unidentified features. Similarly, in liver, we detected 2,269 lipid QTL for 1,190 of the 1,562 (76.2%) traits, of which 927 were from identified lipids while 1,342 were from unidentified features. Fig. 2b and Extended Data Fig. 2c,d present the genetic correlations for this entire collection of substantial QTL extracted in a Manhattan plot. We note that the unidentified molecular traits cluster among the various identified lipid classes, which provides further evidence that these features are of biological origin and amenable for further interrogation. Second, the unidentified features occupy additional distinct loci, implicating previously unidentified lipid classes.

QTL map recapitulates APOA2 biology and informs cholesteryl ester lipid identifications. Several genetic loci are strongly associated with lipids and appear as hotspots: locations on the genome where multiple lipid QTL comap (Fig. 2b and Extended Data Fig. 2b). To better explore these regions, we asked whether these comapping lipid QTL shared a common genetic relationship to segregating alleles at the locus. One advantage of the DO mice is that shared FS allele effect patterns can be indicative of a common genetic regulator[28]. Thus, we define a lipid QTL hotspot as multiple lipid QTL comapping (±2 Mbp) with a shared FS allele effect pattern. We identified a number of hotspots; many of these are detailed in Supplementary Table 1 with their respective lipid class and probable candidate gene drivers. To garner additional support for FS specific genetic effects on lipid abundance, we profiled plasma and liver lipids for each of the FSs (four males, four females; see Supplementary Tables 10 and 11).

Figure 3a highlights a lipid QTL hotspot on chromosome 1:171 Mbp. Here, 255 lipid traits, all from plasma, colocalize with a shared allele effect pattern of upregulation associated with alleles derived from the FS 129 (Extended Data Fig. 3a). The lipid with the highest LOD at this locus was a cholesteryl ester (CE 18:2), which was also elevated in FS 129 plasma (Extended Data Fig. 3b). At 171 Mbp on chromosome 1, strain 129 possesses a missense single nucleotide polymorphism (SNP) in *Apoa2* gene (rs8258226), resulting in a 61Ala>Val substitution in the protein apolipoprotein-II (ref. [40]). A previous DO study identified APOA2 protein and mRNA expression QTL in liver tissue but these displayed different allele effects than plasma lipid QTL, suggesting that the causal variants that modulate their respective levels differ (Extended Data Fig. 3c)[34]. Notably, APOA2 protein is a chief component of high-density lipoprotein (HDL) particles in plasma, corroborated by human HDL traits mapping to APOA2 in GWAS[41], and is considered a principal genetic regulator of plasma HDL levels in mice[42–45]. The other chief components of HDL particles are phospholipids (35–50%) and cholesteryl esters (30–40%) (Fig. 3b)[46]. Consistent with this composition, seven subtypes of phospholipid and various cholesteryl esters map to the *Apoa2* locus (Fig. 3c). Sphingolipids, a minor component of HDL particles, map in four different

Table 1 | Breakdown of lipid identifications in plasma and liver samples by one of 31 classes

			Plasma				Liver			
Lipid category	**Lipid class**	**Abbreviation(s)**	**Count**	**Percentage of IDd (%)**	**Molecular level**	**Percentage of class (%)**	**Count**	**Percentage of IDd (%)**	**Molecular level**	**Percentage of class (%)**
Fatty acyl			**29**	**4.6**	**29**	**100.0**	**37**	**5.9**	**37**	**100.0**
	Acylcarnitine	AC	2	0.3	2	100.0	6	1.0	6	100.0
	Fatty acid[a]	FA	27	4.3	27	100.0	31	5.0	31	100.0
Glycerolipid			**210**	**33.1**	**165**	**78.6**	**185**	**29.7**	**111**	**60.0**
	Diglyceride	DG, alkenyl-DG	2	0.3	2	100.0	17	2.7	15	88.2
	Triglyceride	TG, alkanyl-TG, alkenyl-TG	208	32.8	163	78.4	168	27.0	96	57.1
Phospholipid			**287**	**45.3**	**194**	**67.6**	**303**	**48.6**	**238**	**78.5**
	Cardiolipin	CL	0	0			9	1.4	8	88.9
	Lyso-phosphocholine	LysoPC	27	4.3	27	100.0	18	2.9	18	100.0
	Lyso-phosphoethanolamine	Lyso-PE	5	0.8	5	100.0	10	1.6	10	100.0
	Lyso-phosphoinositol	Lyso-PI	1	0.2	1	100.0	3	0.5	3	100.0
	Phosphocholine	PC	129	20.3	69	53.5	88	14.1	62	70.5
	Phosphoethanolamine	PE, PE-NMe2	24	3.8	22	91.7	80	12.8	57	71.3
	Phosphoglycerol	PG	2	0.3	2	100.0	26	4.2	26	100.0
	Phosphoinositol	PI	23	3.6	19	82.6	23	3.7	21	91.3
	Plasmalogen	Plasmanyl-PC, Plasmenyl-PE, Plasmanyl-PE, Plasmenyl-PC	76	12.0	49	64.5	46	7.4	33	71.7
Sphingolipid			**102**	**16.1**	**41**	**40.2**	**96**	**15.4**	**46**	**47.9**
	Ceramide	Cer[NS], HexCer[NS], HexCer[AP], Cer[NP], Cer[AS], Cer[AP]	40	6.3	34	85.0	58	9.3	39	67.2
	Ganglioside[a]	GM2/GM3	13	2.1	7	53.8	8	1.3	6	75.0
	Sphingomyelin	SM	49	7.7	0	0.0	29	4.7	0	0
	Sphingosine	SP	0	0			1	0.2	1	100.0
Sterol lipid			**6**	**0.9**	**6**	**100.0**	**2**	**0.3%**	**2**	**100.0**
	Cholesteryl ester	CE	6	0.9	6	100.0	2	0.3%	2	100.0
			Count	Percentage of total	Molecular level	Percentage of IDd	Count	Percentage of total	Molecular level	Percentage of IDd
		Identified	634	36.8	**435**	**68.6**	623	39.9	**434**	**69.7**
		Unidentified	1,087	63.2			939	60.1		
		Total	**1,721**	**100.0**			**1,562**	**100.0**		

'Molecular level' refers to lipids identified with individual fatty acid rather than as a sum composition. [a]Hand-identified.

subclasses to this *Apoa2* locus. We conclude that this hotspot illuminates the molecular composition of HDL particles in mice, while also linking an additional 130 unidentified lipid features to this locus.

To test whether a shared QTL would enable identification of additional lipids, we plotted the 255 lipid traits that map to the *Apoa2* locus as a function of chromatographic retention time, mass and identification status (Fig. 3d). A cluster of unidentified lipid features shared retention time with cholesteryl esters, a class of lipids that are often devoid of informative fragments[47]. All cholesteryl esters showed their main QTL at the *Apoa2* locus (Fig. 3e) providing greater confidence in their identification. The shared genetic regulation further allowed us to predict a cholesteryl ester identity for the cluster of unidentified comapping features. Examination of their total masses[48] and tandem mass spectra supported the annotation of five additional cholesteryl esters (Fig. 3f), while another 18 lipid features' *m/z* and retention time were consistent with technical artefacts of cholesteryl esters: 11 heterodimers, four cholesterol adducts and three in-source fragments.

QTL map provides an orthogonal tool for lipid identification. On chromosome 10, at 127 Mbp we observed a notable lipid QTL hotspot. At this site, over 25 plasma and liver lipid features mapped with the highest overall importance (Fig. 4a). These features also shared a common allele dependence, that is, NOD-driven and split between NOD high versus low effect (Fig. 4b). None of these lipid features were identified following our conventional data analysis strategy, which leverages retention time, mass and tandem mass spectra. The features were observed in two distinct clusters on the basis of *m/z* and retention time, suggesting they could derive from two distinct lipid classes (Fig. 4c). Given that these unidentified features (1) appeared as two defined lipid classes and (2)

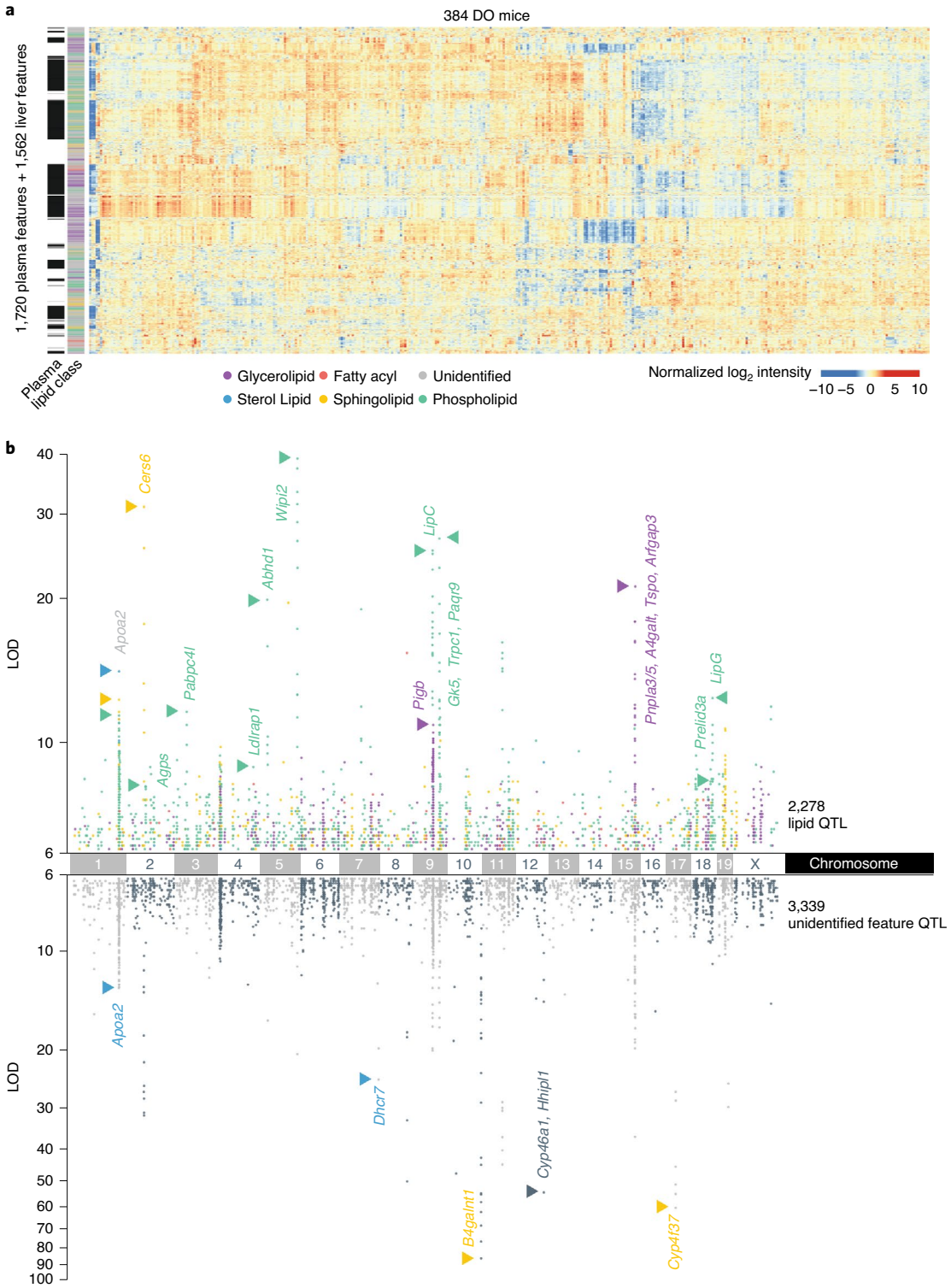

Fig. 2 | Large-scale lipid quantitative profiling and subsequent QTL mapping reveals hotspots of associated lipids. a, In plasma, we quantified 1,721 lipidomic features, 621 of which were identified, and in liver, we quantified 1,562 lipidomic features, 615 of which were identified. Hierarchical clustering of all 3,283 lipidomic features' intensities by the 384 DO mice resulted in distinct clustering by lipid class, notably across tissue type. **b**, When mapped onto the mouse genome, 1,405 plasma and 1,190 liver features showed at least one QTL with an LOD > 6 as displayed in a Manhattan plot ($n = 3,353 + 2,269 = 5,622$ total QTL). A number of lipid hotspots are shared by identified lipids and unidentified features (for example, at *Apoa2*), while others only appear among the unidentified features (for example, at *B4galnt1*). Chr, chromosome.

were high scoring at a genetic locus with opposite allele effects, we reasoned that identification of the causal gene may enable their identification.

The genetic effects of SNPs and other genomic variants can influence lipid abundance. For example, SNPs in coding regions can affect protein product function. In the extreme, a missense variant

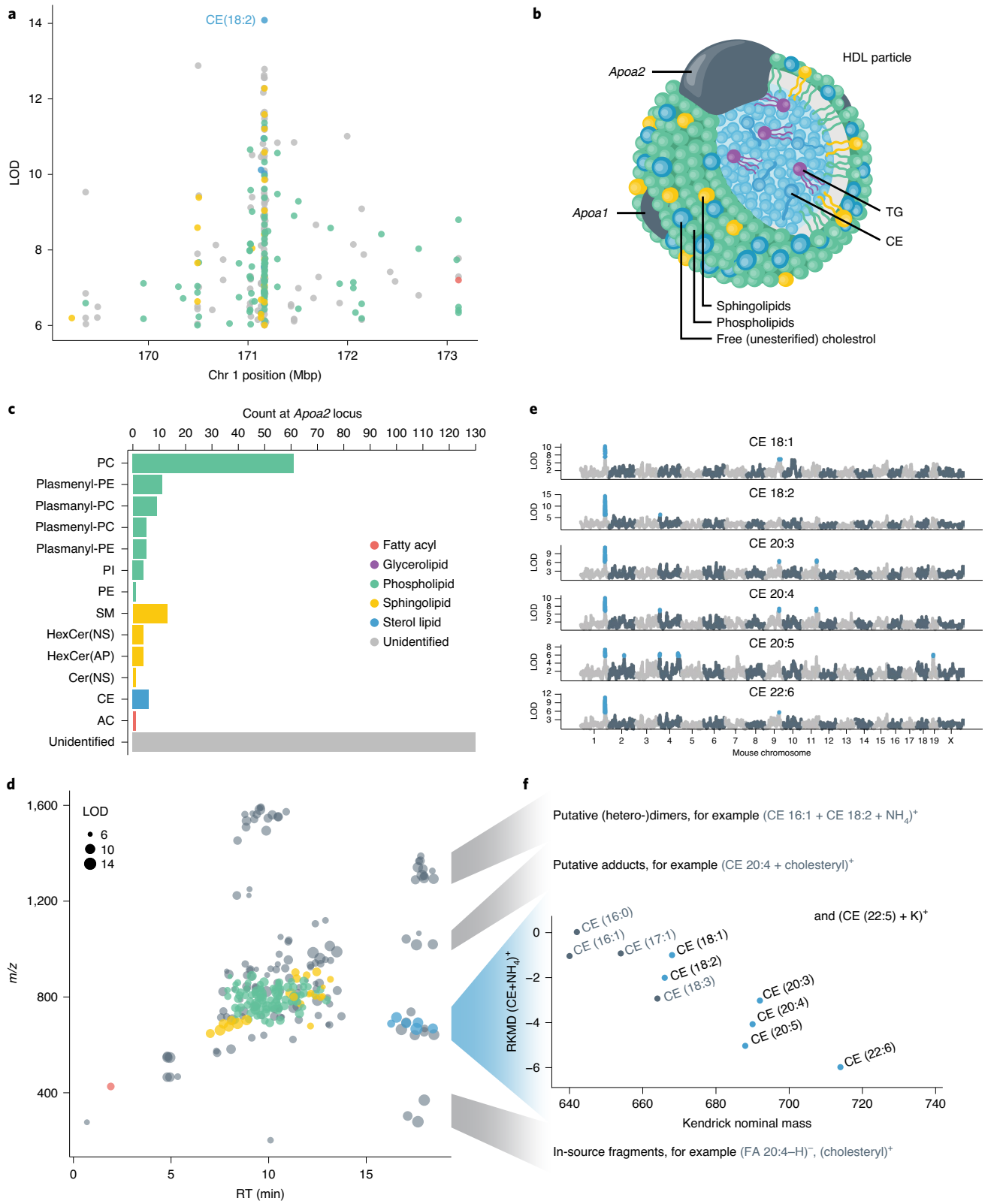

Fig. 3 | Comapping of lipids at the *Apoa2* locus facilitated identification of additional cholesteryl esters. a, One lipid hotspot on chromosome 1 at 171 Mbp is shared by 255 plasma lipid features comapping with a common 129 high allele effect (Extended Data Fig. 3a). **b**, The candidate gene at this locus is *Apoa2*, which encodes apolipoprotein-II, which is carried on HDL cholesterol particles along with **c**, a variety of lipid classes, mostly phospho- and sphingolipids, which mapped to the locus. **d**, When plotting all 255 *Apoa2*-specific lipid features in the *m/z*–retention time (RT) plane, a group of unidentified features sharing the RT region with cholesteryl esters (CEs) stood out. **e**, Notably, all six CEs show their primary QTL at this locus, as visible from their individual LOD plots. **f**, Subsets of the unidentified features could subsequently be identified as CE-related features, including heterodimers, cholesterol adducts and in-source fragments. FA (fatty acid), PE (phosphatidylethanolamine), PI (phosphatidylinositol), RKMD (referenced Kendrick mass defect)[48].

in proteins involved in lipid metabolism could probably affect lipid abundance. SNPs in non-coding regions, such as promoters and enhancers, can alter gene expression. To identify candidate SNPs, we analysed the SNPs associated with the lipids by identifying those with the FS SNP database at each QTL (R/qtl2, scan1snps()[27]) and subsequently causing missense, frameshift, stop lost/gained, incomplete terminal codons, in-frame deletions/insertions, altering 3′ or 5′ untranslated region (UTR) sequences, splice acceptor/donor/region, predicated to cause nonsense-mediated decay, initiator codon or mature miRNA variants (according to the Sequence Ontology consortium)[49]. At the chromosome 10 hotspot, we identified several candidate genes with potentially causal mutations (Fig. 4d). We included in our analysis, but did not focus on genes with synonymous, stop retained, upstream/downstream, intergenic, intron and non-coding transcript (exon) variants (which represent ~97% of all SNPs in the database).

In cases of altered gene expression, we further narrowed down the list of candidates by directly assessing transcriptomics data. While we did not profile hepatic gene expression in the DO cohort used for lipid QTL analysis, we surveyed a recently published hepatic QTL dataset to match allele effects of mRNA expression and protein QTL that are within the location of the candidate gene (*cis*-eQTL and pQTL, respectively)[34]. We asked if any transcripts or proteins presented a similar NOD-driven allele effect at the lipid locus on chromosome 10. Of the protein coding genes within ±2 Mbp of the lipid QTL, 55 showed a *cis*-eQTL (Supplementary Table 2). However, the only *cis*-eQTL that was strongly and uniquely driven by NOD alleles was *B4galnt1* (Extended Data Fig. 4a). Furthermore, 16 *cis*-pQTL were identified for genes within this region, including B4GALNT1 (Supplementary Table 3). Similarly to the cis-eQTL, the only pQTL that showed a NOD-driven allele effect pattern was for B4GALNT1 (Extended Data Fig. 4b). Consequently, the 3′ UTR variant in *B4galnt1* SNP rs13462597 was our strongest candidate as the genetic regulation of hepatic *B4galnt1* transcript and protein expression matches that of the unidentified lipids.

B4galnt1 encodes β-1,4 *N*-acetylgalactosaminyltransferase 1, an enzyme that catalyses the conversion of GM3 to GM2 gangliosides[50]. With this candidate gene in mind, we investigated whether the unidentified lipids could be classified as gangliosides. Their precursor *m/z* and tandem mass spectra were consistent with monosialic gangliosides, which we further confirmed by comparison with a GM3 ganglioside standard (Fig. 4e). In total, we confidently identified 26 lipid features as six unique GM2 and seven unique GM3 species (Supplementary Table 4). In agreement with a NOD-driven effect, NOD mice have higher abundance of GM3 gangliosides in the pancreas[51] and we confirmed NOD had higher abundance of GM3 in plasma in an independent lipidomic analysis of FS mice (Extended Data Fig. 4c).

By identifying the features mapping to chromosome 10:127 Mbp as gangliosides, we recognized that ganglioside abundances, such as the levels of most lipid species, were polygenic, that is, regulated by multiple loci (Fig. 4f). From the 26 identified ganglioside features we gain a total of 62 QTL annotations, describing more than 15 unique loci (at least two ganglioside features with LOD > 6.0) on ten chromosomes (Supplementary Table 5). These newly annotated ganglioside QTL mapped to candidate genes of the ganglioside pathway (*Sgms1*, ref. [52]; *B3galt4*; *St3gal2*; *Cmah*[53]), even more distant regulators of ganglioside metabolism (*Slc9a6*, ref. [54]; *Cog2*, ref. [55]; *Trcp5*, ref. [56]; *Cdh13)* and regions of the genome with yet undescribed ganglioside regulation (Fig. 4g).

LipidGenie identifies candidate genetic regulators for lipid features. To make these genome–lipid associations accessible to the community we created a web-based resource, LipidGenie (http://lipidgenie.com). With LipidGenie, lipid features can be searched by *m/z*, lipid identifier or lipid class. The search returns QTL of the matching features and allows the user to explore the genetic region, FS allele effects and associated SNPs. In addition, with LipidGenie individual genes or gene regions can be queried for lipid associations.

To validate LipidGenie we explored sex-associated lipid features that were observed within the B6 FS. In this study, we quantified 2,558 lipid features in B6 plasma and found 254 features that showed notably different levels by sex (Fig. 5a). As is common in LC–MS lipidomics, most of these sex-specific features were unidentified after the database search ($n = 197$). Using LipidGenie's *m/z* search parameter and a 10 ppm *m/z* window, we found notable genome–lipid associations for 127 of the sex-specific features, of which 79 were unidentified. A group of six unidentified lipids mapped to the same genetic locus on chromosome 6 at 91 Mbp (Fig. 5b and Supplementary Table 6); all had similar allele effect patterns (Extended Data Fig. 5a) and were elevated in males (Fig. 5a and Extended Data Fig. 5b). At the locus, a total of 12 out of 21 comapping features shared a lipid class-like behaviour, that is, clustered in *m/z*–RT space (Fig. 5c). To further characterize these lipids, we collected additional tandem mass spectra in both positive and negative mode (Fig. 5d–g).

The spectra showed shared fragmentation patterns consistent with a phosphatidylcholine (PC) class identity. One fatty acid seemed to be either fatty acid 22:6 (Fig. 5e) or fatty acid 16:0, but only MS3 spectra showed the presence of a second acyl-chain expected for PCs (Fig. 5f,g). These features also shared an *m/z* 522 fragment that matched the formula of LysoPC 19:0, $C_{26}H_{53}NO_7P^-$.

We next used the LipidGenie associations to generate hypotheses about the nature of this lipid class. At chromosome 6 at 91 Mbp, we found SNPs with matching allele effects in several genes including *Txnrd3*, *Vmn1r*, *Uroc1*, *Aldh1l1*, *Slc41a3*, *Grip2* and *Trh* (Fig. 5b). One possible candidate on chromosome 6 is *Vmn1r*, encoding for vomeronasal receptors, the organs that sense pheromones. This gene explained the observed sex difference and also points to PC estolides as a potential class identity. Estolides are lipids containing fatty acid esters of hydroxy-fatty acids (FAHFAs). Consistent with the observed 16:0 or 22:6 fragments in MS2 spectra of the unidentified lipids, 16:0 and 22:6 can be esterified to hydroxy-fatty acids to form FAHFAs[57]. This hypothesis is further supported by accounts of FAHFAs as pheromones in spiders and triglyceride estolides in mammalian scent glands[58]. The potential estolide identity is intriguing, but definitive identification will require follow-up studies. Further evidence is probably contained in the genetic associations. Similar to our earlier example with gangliosides, we observed comapping of these 12 lipids at other loci (for example, Chr 1, at

Fig. 4 | Lipid features mapping to *B4galnt1* lead to identification of GM2 and GM3 gangliosides. a,**b**, A hotspot of solely unidentified features with exceptionally strong correlation was composed of 11 liver and 15 plasma features mapping to chromosome 10:127 Mbp (**a**) with a similar NOD-driver allele pattern (**b**) (two main clusters from hierarchical clustering, row-scaled, Euclidean cutoff of $h = 2.5$). **a**–**c**, Two groups of lipid features (circles versus triangles) emerged as distinct in strength of LOD (**a**), directionality of allele effect (**b**) and *m/z* space (**c**). **d**,**e**, The candidate gene *B4galnt1* pointed us to the putative identifications of GM3 (circles) and GM2 (triangles) gangliosides (**d**), which were confirmed by spectral matching with a human GM3 standard (**e**). **f**, Secondary QTL for these gangliosides, as exemplary shown for GM2 d18:1_22:0, mapped to eight additional candidate genes within 4 Mbp of the 15 total ganglioside hotpots that were previously linked to ganglioside metabolism. **g**, The various candidate genes influencing GM3 and GM2 levels span well-known enzymes (for example, B3galt4) but also include indirect affecters including Cog2 and Slc9a6. NOD (mouse strain NOD/ShiLtJ), Glc (glucose), GalNAc (*N*-acetylgalactosamine), Gal (galactose), NGNA (*N*-glycolylneuraminic acid), NANA (*N*-acetylneuraminic acid).

84 Mbp, Chr 12 at 84 Mbp), thereby offering potential pathway information (Supplementary Table 7) and highlighting the power of genome–lipid associations obtained with LipidGenie.

We next explored whether LipidGenie would also offer insights when querying for identified lipid features. Recently, Parker et al. found an association between LysoPC 14:0 and chromosome 5

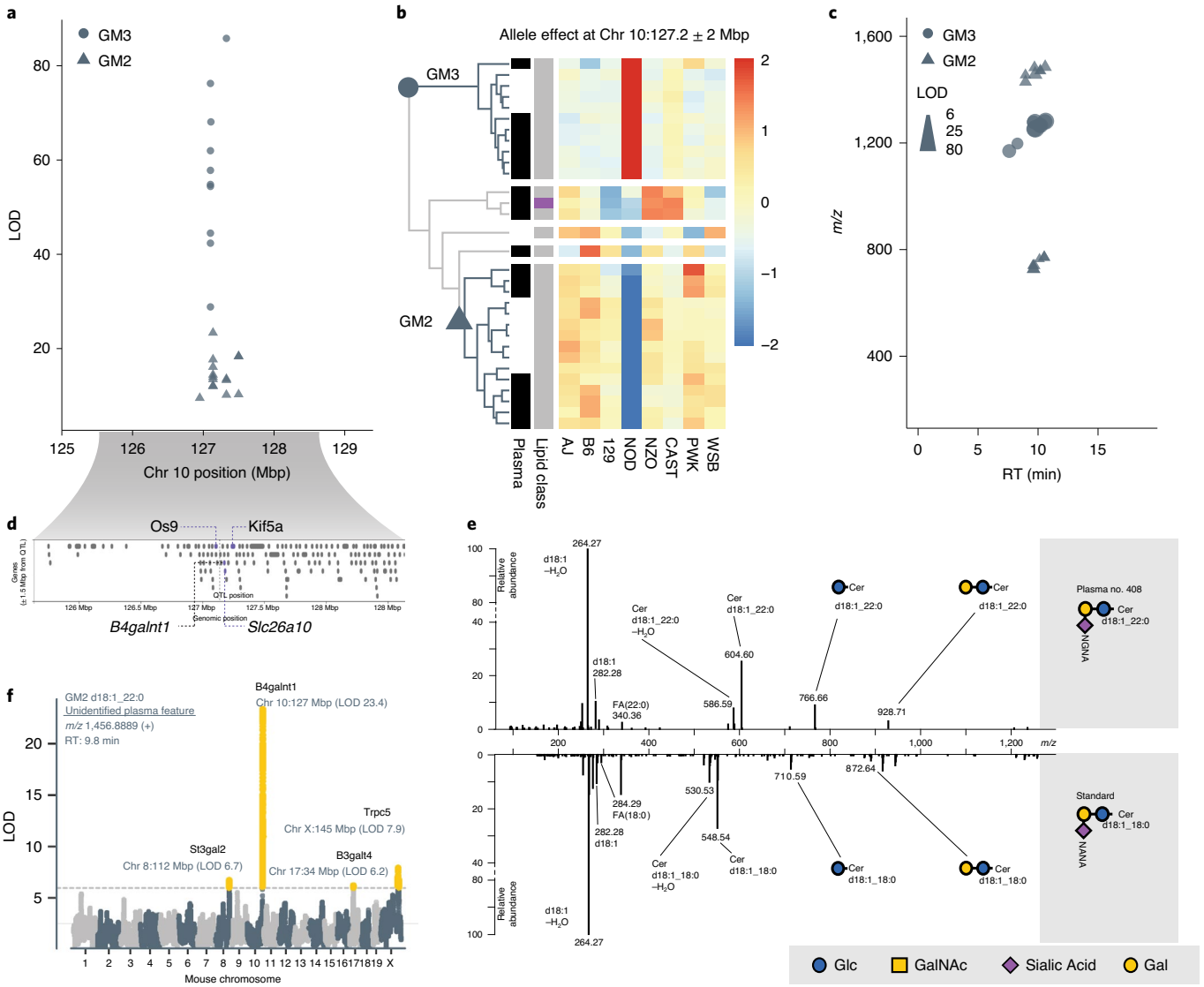

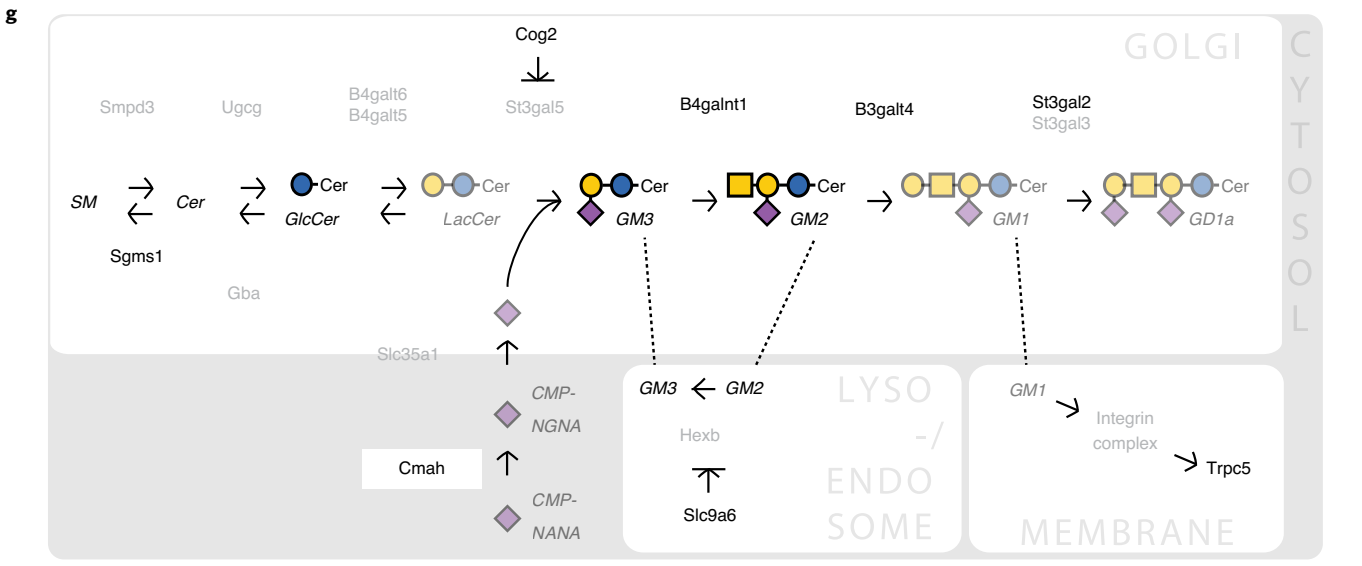

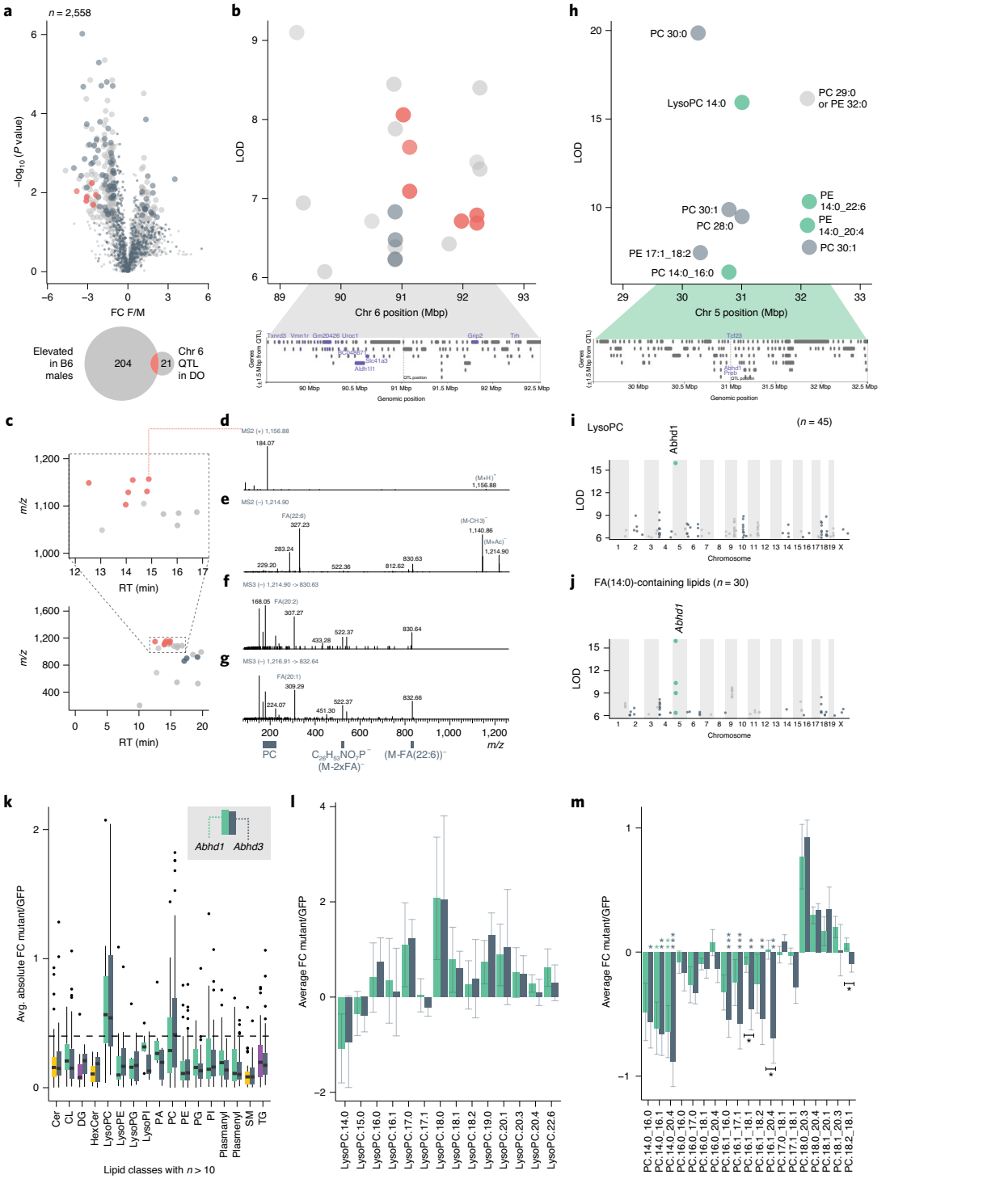

Fig. 5 | Web resource LipidGenie guides exploration of genome–lipid connections. a, We quantified 2,558 features in B6 plasma ($n = 4$ for each sex). 254 features were sex-specific (fold change (FC) > 1.0, $P < 0.05$, non-paired, two-sided Student's *t*-test). Precursor *m/z* (±10 ppm) matching to our DO database provided genetic information for one-third of the otherwise unidentified features. **b**, Six male-specific unidentified features (red) share a QTL on Chr 6:91 Mbp with a common A/J down effect (Extended Data Fig. 5a). **c**, The features further clustered in *m/z*–RT space. **d**–**g**, Targeted fragmentation spectra (exemplary spectra for two species ($[M+H]^+$ *m/z* 1,156 (**d**–**f**) and 1,158 (**g**)) in positive (MS2) (**d**) and negative (MS2 (**d**,**e**) and MS3 (**f**,**g**)) mode) exhibited signals consistent with a lipid class built of a PC headgroup and three FAs. **h**–**k**, The DO database further confirmed LysoPC 14:0 mapping to *Abhd1* (ref. [59]) (**h**) with an enrichment of fatty acid 14:0 (**j**) containing lipids (**k**), We compare Hepa1-6 overexpressing *ABHD1* and *ABHD3* versus a control overexpressing GFP ($n = 12$ for each, four biological × three technical replicates, boxplots are defined with first and third quartiles for lower and upper hinges, 1.5× interquartile range for the length of the whiskers, centre line at median). The boxplots show absolute FC of each mutant over GFP by lipid class; the dashed line is at FC of 0.4. **l**, The lowest (negative) FC for both is observed for LysoPC 14:0; isomers are summed. **m**, All 14:0-containing PCs exhibit a negative FC for *ABHD1* and *ABHD3* mutants consistently, while 18:0-containing species are showing opposing positive FC. Plotted are sum-normalized, $\log_2$-transformed FC means with error bars representing 95% confidence interval, significance indicated by $^*P < 0.05$, $^{**}P < 0.01$, $^{***}P < 0.001$ of non-paired two-sided Student's *t*-test, equal variance, $n = 12$ for each, details in-source data. F/M (female-to-male).

at 31 Mbp using multi-omic QTL mapping of the hybrid mouse diversity panel[59]. From these data, they postulated that the protein encoded by candidate gene *Abhd1* (alpha beta hydrolase domain containing 1) regulates plasma levels of LysoPCs. Of note, ABHD1 has no annotated function. LipidGenie's lipid search provides a direct means to test this putative functional annotation of ABHD1.

LipidGenie confirmed that plasma LysoPC 14:0 has a strong QTL at the *abhd1* locus (Fig. 5h), and further found the B6 and NZO high-allele effect consistent with the 3′ UTR variant rs29681817 (Extended Data Fig. 5c). This observation is further supported by an independent measure of the FS mice and a hepatic *cis*-eQTL in *Abhd1* with matching opposite allele effects (Extended Data Fig. 5d, e). To connect the function of ABHD1 protein to LysoPCs, we asked whether other LysoPCs ($n=45$) mapped to this gene region. However, we did not find general mapping of LysoPCs to this locus (Fig. 5i), but instead found other lipids comapping on chromosome 5, at 31 Mbp, including PC 14:0_16:0, PE 14:0_20:4, PE 14:0_22:6, PC 28:0, PC 30:0 and PC 30:1 (Fig. 5h). These fatty acid signatures suggest a myristic acid (14:0) specific association. Given the high degree of lipid structural resolution contained within LipidGenie, we demonstrate that 14:0-containing lipids ($n=30$) have an enriched hotspot at the *Abhd1* locus (Fig. 5j). With these data we propose that ABHD1 is a phospholipase for myristic acid containing phospholipids, consistent with the function of a related and highly homologous gene, *abhd3* (refs. [60,61]). Phospholipids containing 14:0 have also been mapped to ABHD3 in human GWAS[62]. To validate this hypothesis, we overexpressed ABHD1 and ABHD3 in Hepa1-6 cells (Extended Data Fig. 6a,b) and measured their lipidome with respect to cells overexpressing green fluorescent protein (GFP) as control (Supplementary Table 12). Hierarchical clustering of the top 49 features showed two clusters, one with increased levels in the mutants over control and the other one decreased (Extended Data Fig. 6c). We noticed most of the identified lipids among the most substantially different features, and when plotting the average fold change by lipid class, LysoPC and PC phospholipids stood out (Fig. 5k). On closer examination, we were able to confirm the predicted fatty acid dependency for both LysoPC and PC lipids, particularly prominent in 14:0-containing phospholipids (Fig. 5l,m). While ABHD1 and ABHD3 mutants exhibited largely similar lipidomic profiles, differences as in PC 16:1_20:4, which was decreased only in the Abhd3 mutant, may also point to differential functions. The 14:0 specificity could be relevant to human health as plasma LysoPC 14:0 is a predictor of diabetes risk in humans. Finally, our proposed function might provide a clue to understanding why ABHD1 is associated with oxidative stress, a prominent hallmark of metabolic diseases[60,63,64].

Having documented the diverse use of LipidGenie for lipid queries, we finally tested its use for gene-based queries. ABHD2, another member of the alpha beta hydrolase domain protein family, acts on arachidonylglycerol, among other substrates[65,66]. A LipidGenie query of *Abhd2* does indeed provide evidence for this polyunsaturated fatty acid pathway specificity. Specifically, within 2 Mbp of *Abhd2*, LipiGenie returned ten liver phospholipids. Eight of these lipids shared an allele effect pattern, and contained polyunsaturated fatty acids; that is, 18:2, 18:3, 20:3, 20:4 and 22:6 (Extended Data Fig. 5f,g). Further, ABHD2 showed matching opposite WSB and CAST effects in both liver *cis*-eQTL and pQTL (Extended Data Fig. 5h,i)[34].

Discussion

Discovery lipidomics currently relies on measurement of various chemical properties for lipid identification. These properties are most often hydrophobicity, mass and fragmentation pattern. Unfortunately, application of only these strategies to complex mammalian lipid mixtures results in many unidentified lipid features. Here we investigated the power of genome–lipid associations to facilitate lipid identification.

To construct a large-scale map of genome–lipid associations, we performed QTL analysis for over 5,000 plasma and liver lipid QTL, of which over 60% stem from unidentified spectral features. To our knowledge, this QTL map is the broadest in scope and depth of lipids analysed and QTL identified in mice[59,67,68]. With these data, we first tested our hypothesis by analysing one of several QTL hotspots, the *Apoa2* locus. The identified lipids mapping to this locus belonged to 11 different classes and, together with APOA2, constitute the known components of HDL particles. With this association, 23 unidentified lipid features could be classified as cholesteryl esters and related features.

To further test the concept, we selected a second hotspot containing only unidentified lipid features (chromosome 10:127 Mbp). Genetic mapping to *B4galnt1* enabled their identification as GM3 and GM2 gangliosides. In fact, the identification allowed for a comprehensive investigation of their complex polygenic regulation. We identified a total of eight candidate genes that probably contribute different functions in the pathway, including three (*Slc9a6*, *Cog2*, *Trpc5*) that exert indirect effects on ganglioside biosynthetic enzymes.

Having confirmed the value of genome–lipid associations for lipid mass spectral data annotation, we built an interactive, queryable resource, LipidGenie. Using the lipid query function, we demonstrated LipidGenie's ability to facilitate lipid identification and in one instance revealed a potentially new subclass of PC lipids (PC estolides). Beyond assisting lipid identification, LipidGenie can provide evidence for gene function, and when queried for either lipid or gene identity, LipidGenie revealed acyl-chain specificity for ABHD1 and ABHD2, respectively. We confirmed the putative phospholipase function of ABHD1 in cells overexpressing the mouse protein while comparing to ABHD3.

We envision the genome–lipid associations contained within LipidGenie to be a valuable resource for researchers across multiple fields. We anticipate it will be immediately useful for directed analysis of key unidentified features in exploratory lipidomics analyses and lead to recovery of more data for biological studies. A limitation of the approach is that lipid identification remains a manual process and this tool does not remove the requirement for expert knowledge and care in spectral interpretation for its use. With all this said, we hope it will garner excitement for potentially new genetic regulation of lipid metabolism. Finally, through integration with other large data resources, for example, protein–protein interactions, pathway tools, tissue-specific QTL, GWAS data and so on, these genome–lipid associations will allow more global integration of lipid data into current knowledge bases. Especially the integration with human loci will allow for cross-validation to provide information on human health and disease[69,70].

Methods

Animal husbandry and sample collection. All experiments involving mice were preapproved by an AAALAC-accredited Institutional Animal Care and Use Committee of the College of Agricultural Life Sciences (CALS) at the University of Wisconsin–Madison. The CALS Animal Care and Use Protocol number associated with the study is A005821, A.D. Attie, Principal Investigator. Equal numbers of male and female DO mice and the eight FSs (C57BL/6J (B6), A/J, 129S1/SvImJ (129), NOD/ShiLtJ (NOD), NZO/HILtJ (NZO), PWK/PhJ (PWK), WSB/EiJ (WSB) and CAST/EiJ (CAST)) were all obtained from the Jackson Laboratories and have been previously described[32,33,71]. Briefly, all mice were housed within the vivarium at the Biochemistry Department, University of Wisconsin–Madison, and maintained on a Western-style high-fat/high-sucrose diet (44.6% kcalories of fat, 34% carbohydrate and 17.3% protein) from Envigo Teklad (TD.08811) for 16 weeks. All mice were maintained in a temperature and humidity-controlled room on a 12 h light/dark cycle (lights on at 6:00 and off at 18:00), and provided water ad libitum. At ~22 weeks of age, mice were killed following a 4-h fast. Plasma and liver were collected from each mouse and flash frozen in liquid nitrogen. One sample from each tissue per mouse was used for lipidomic analyses.

Mouse genotyping and haplotype reconstruction. We collected tail biopsies for DNA extraction[28] at 4–6 weeks of age when animals arrived at the University of

Wisconsin and were assigned to single-housed pens. We shipped DNA to Neogen for genotyping using the Mouse Universal Genotyping Array (GigaMUGA, 143,259 markers). Genotype calls were subject to quality control as described in Broman et al.[72]. Genotypes were used to reconstruct the eight-founder haplotype mosaic of each DO mouse using the hidden Markov model in the R/qtl2 software package[27,32]. The haplotype reconstruction uses information at each genetic markers and its neighbours to assign an eight-state haplotype probability that accounts for both heterozygosity and uncertainty in haplotype assignments[26]. We interpolated the founder haplotype probabilities onto an evenly spaced grid of 69,005 pseudo-markers for mapping analysis. Sample mix-ups (one pair of samples) were resolved using islet gene expression data as described in Keller et al.[73].

Plasmids and cell culture expression. Mouse Abhd1 (CMV6 promoter, Myc-DDK-tagged, MR206471) and mouse Abhd3 (CMV6 promoter, Myc-DDK-tagged, MR206458) plasmids were obtained from Origene. The manufacturer's sequencing primers were used to confirm plasmid insertion. His-tagged CMV6-GFP plasmid was a gift from J. Simcox. All plasmids were transformed into *Escherichia coli* (ThermoFisher Scientific, 18258012). Plasmids were maxiprepped according to the manufacturer's instructions (Qiagen, 12362).

Then 5×10^5 Hepa1-6 cells (ATCC CRL-1830) were seeded in six-well plates with DMEM (ThermoFisher Scientific, 12100061). After 16 h, cells were reconditioned with fresh medium for 2 h. Cells were transfected in triplicate with Lipofectamine2000 (ThermoFisher Scientific, 11668019) according to the manufacturer's instructions. Transfection efficiency was confirmed by visualizing GFP. After 24 h, medium was replaced. Then, 48 h after transfection, cells were washed in cold 1× PBS and scraped to be released from the plate. Released cells were pelleted by centrifugation and snap-frozen in liquid nitrogen. The frozen cell pellets were stored at −80 °C until lysis. Hepa1-6 cells were a gift from J. Simcox.

For western blots, cell pellets were lysed in 2× SDS–PAGE loading buffer and boiled at 95 °C for 5 min. Samples were run on a 10% SDS–PAGE gel for 1.5 h at 120 V, standard is Precision Plus Dual Color Protein Standards (Bio-Rad, 1610394). Samples were wet-transferred onto polyvinyldifluoride membrane (Bio-Rad, 1620177) for 1.5 h at 100 V. Following transfer, membrane was blocked in 5% milk in tris-buffered saline and polysorbate 20 (TBST) for 1 h at room temperature. Membrane was incubated overnight at 4 °C with 1:2,000 rabbit anti-MYC antibody (CST, 2,278 clone 71D10) in blocking buffer. Primary antibody was removed by washing three times with 1× TBST. Membrane was incubated with 1:2,000 goat antirabbit-HRP conjugated antibody (CST, 7074S) in blocking buffer. Samples were visualized with Clarity Western ECL Substrate (Bio-Rad, 1705060) on a ThermoFisher iBright FL1500 Imaging System. Uncropped and unprocessed scans are supplied in the Source Data file.

Lipidomics sample preparation. *Plasma.* Here, 40 µl (30 µl for FSs, FS) of plasma and 10 µl of SPLASH Lipidomix internal standard mixture (Avanti Polar Lipids) were aliquoted into a tube. Protein was precipitated by addition of 215 µl of MeOH. Control samples comprised an aliquot of mixed male and female B6 plasma (Chow diet), extracted with each batch. After the mixture was vortexed for 10 s, 750 µl methyl-*tert*-butyl ether (MTBE) were added as extraction solvent and the mixture was vortexed for 10 s and mixed on an orbital shaker for 6 min. Phase separation was induced by adding 187.5 µl of water followed by 20 s of vortexing. All steps were performed at 4 °C on ice. Finally, the mixture was centrifuged for 4 min at 14,000*g* at 4 °C and 150 µl of the lipophilic upper layer were transferred to glass vials and dried by vacuum centrifuge for 60 min. The dried extracts were resuspended in 100 µl of MeOH/Toluene (9:1, v/v).

Liver. Here, 20 (±2) mg of liver tissue, frozen in liquid nitrogen along with 20 µl of SPLASH Lipidomix internal standard mixture were aliquoted into a tube with a metal bead and 1150 µl of MTBE/MeOH (10:3, v/v) were added for protein precipitation. Control samples for DO comprised aliquots of sample pooled from FS, extracted with each batch. All steps were performed at 4 °C on ice. The mixture was homogenized by bead beating for 4 min at 25 Hz and shaking on an orbital shaker for 6 min. After bead removal, 225 µl of water were added to each tube and the mixture was vortexed for 20 s. Finally, the mixture was centrifuged for 20 min at 13,000*g* at 4 °C after which 200 µl of the lipophilic upper layer were transferred to glass vials and dried by vacuum centrifuge for 60 min. The dried lipophilic extracts were resuspended in 100 µl of MeOH/toluene (9:1, v/v).

Cells. Hepa1-6 cells were scraped off of six-well plates and transferred to 1.5-ml Eppendorf tubes. Cell pellets were kept frozen (less than −20 °C) until extraction. Cells were lysed and protein was precipitated by addition of 225 µl of MeOH. Then 750 µl methyl-*tert*-butyl ether (MTBE) were added as extraction solvent. The mixture was homogenized by vortexing for 10 s and shaking on an orbital shaker for 6 min. Phase separation was induced by adding 187.5 µl of water followed by 20 s of vortexing. All steps were performed at 4 °C on ice. Finally, the mixture was centrifuged for 8 min at 14,000*g* at 4 °C and 200 µl of the lipophilic upper layer were transferred to glass vials and dried by vacuum centrifuge for >60 min. The dried extracts were resuspended in 100 µl of MeOH/toluene (9:1, v/v).

LC–MS/MS. Sample analysis by LC–MS/MS, running data-dependent acquisition with dynamic exclusion and polarity switching, was performed in randomized order on an Acquity CSH C18 column held at 50 °C (2.1 mm × 100 mm × 1.7 µm particle diameter, Waters) using an Ultimate 3000 RSLC Binary Pump (400 µl min^{-1} flow rate, Thermo Scientific) for plasma, while for the liver and cell samples a Vanquish Binary Pump (400 µl min^{-1} flow rate, Thermo Scientific) was used. Mobile phase A consisted of 10 mM ammonium acetate in ACN/H_2O (70:30, v/v) containing 250 µl l^{-1} of acetic acid. Mobile phase B consisted of 10 mM ammonium acetate in IPA/ACN (90:10, v/v) with the same additives. Mobile phase B was initially held at 2% for 2 min and then increased to 30% over 3 min. Mobile phase B was further increased to 50% over 1 min and 85% over 14 min and then raised to 95% over 1 min and held for 7 min. The column was re-equilibrated for 2 min before the next injection.

Plasma. Ten microlitres of lipid extract were injected through SII for Xcalibur by an Ultimate 3000 RSLC autosampler (Thermo Scientific). The LC system was coupled to a Q Exactive Focus mass spectrometer run by Tune software v.2.5.0.2042 (Thermo Scientific) by a HESI II heated ESI source kept at 300 °C (Thermo Scientific). The inlet capillary was kept at 300 °C, sheath gas was set to 25 units, auxiliary gas to 10 units, and the spray voltage was set to 5,000 V(+) and 4,000 V(−), respectively. The MS was operated in polarity switching mode acquiring positive and negative mode MS1 and MS2 spectra (Top2) during the same separation. MS acquisition parameters were 17,500 resolving power, 1×10^6 automatic gain control (AGC) target for MS1 and 1×10^5 AGC target for MS2 scans, 100-ms MS1 and 50-ms MS2 ion accumulation time, 200- to 1,600-Th MS1 and 200- to 2,000-Th MS2 scan range, 1-Th isolation width for fragmentation, stepped higher-energy collision dissociation (HCD) collision energy (20, 30, 40 units), 1.0% under-fill ratio and 10-s dynamic exclusion.

Liver. One microlitre of lipid extract was injected through SII for Xcalibur (Thermo Scientific) by a Vanquish Split Sampler HT autosampler (Thermo Scientific). The LC system was coupled to a Q Exactive HF mass spectrometer run by Tune software v.2.8.0.2688 (Thermo Scientific) by a HESI II heated ESI source kept at 300 °C (Thermo Scientific). The inlet capillary was kept at 300 °C, sheath gas was set to 25 units, auxiliary gas to 10 units, and the spray voltage was set to 4,000 V(+) and 3,500 V(−), respectively. The MS was operated in polarity switching dd-MS2 mode acquiring positive and negative mode MS1 and MS2 spectra (Top2 for positive, Top3 for negative mode) during the same separation. MS acquisition parameters were 60,000 resolution and 3×10^6 AGC target for MS1 and 15,000 resolution and 5×10^5 AGC target for MS2 scans, 100-ms MS1 and 35-ms MS2 ion accumulation time, 240 to 1,200-Th MS1 scan range for positive and to 1,600-Th for negative mode, and 200- to 2,000-Th MS2 scan range, 1.4-Th isolation width for fragmentation, stepped HCD collision energy (20, 25 units for positive; 20, 30 units for negative mode) and 10-s dynamic exclusion.

Cells. Ten microlitres of lipid extract were injected through SII for Xcalibur (Thermo Scientific) by a Vanquish Split Sampler HT autosampler (Thermo Scientific). The LC system was coupled to a Q Exactive HF mass spectrometer run by Tune software v.2.9.3.2948 (Thermo Scientific) by a HESI II heated ESI source kept at 300 °C (Thermo Scientific). The inlet capillary was kept at 300 °C, sheath gas was set to 25 units, auxiliary gas to 10 units, and the spray voltage was set to 4,000 V(+) and 3,500 V(−), respectively. The MS was operated in polarity switching mode acquiring positive and negative mode MS1 and MS2 spectra (Top2) during the same separation. MS acquisition parameters were 30,000 resolving power, 1×10^6 AGC target for MS1 and 1×10^5 AGC target for MS2 scans, 100-ms MS1 and 50-ms MS2 ion accumulation time, 200- to 1,600-Th MS1 scan range, 1-Th isolation width for fragmentation, stepped HCD collision energy (20, 30, 40 units), 1.0% under-fill ratio and 10-s dynamic exclusion.

Lipidomics data analysis. The resulting LC–MS lipidomics raw files were converted to .mgf files via MSConvertGUI (ProteoWizard, P. Mallick, Stanford University[74]) and processed using Compound Discoverer v.2.0 (ThermoFisher Scientific) and an in-house developed open-source software suite, LipiDex[16]. Briefly, these software tools use area under the peak intensity calculations to generate relative quantitation of each spectral feature as is typical for metabolomic analyses. All raw files were loaded into Compound Discoverer with blanks marked as such to generate two result files using the following Workflow Processing Nodes: Input Files, Select Spectra, Align Retention Times, Detect Unknown Compounds, Group Unknown Compounds, Fill Gaps and Mark Background Compounds for the so called 'Aligned' result and solely Input Files, Select Spectra, and Detect Unknown Compounds for an 'Unaligned' Result. Under Select Spectra, the retention time limits were set between 0.4 and 21 min, MS order as well as unrecognized MS order replacements were set to MS1. Under Align Retention Times the mass tolerance was set to 10 ppm and the maximum shift according to the dataset to 0.5 min. Under Detect Unknown Compounds, the mass tolerance was also set to 10 ppm, with an signal-to-noise threshold of 3, and a minimum peak intensity of 5×10^5 (DO) or 1×10^5 (FS, Cells). Further, $[M+H]^{+1}$ and $[M-H]^{-1}$ were selected as ions ($[M+H]^{+1}$ and $[M-H+TFA]^{-1}$ for cells) and a maximum peak width of 0.75 min as well as a minimum number of scans per

peak equal to five were set. Last, for Group Unknown Compounds as well as Fill Gaps, mass tolerance was set to 10 ppm and retention time tolerance to 0.2 min. For best compound selection rules nos. 1 and 2 were set to unspecified, while MS1 was selected for preferred MS order and $[M+H]^{+1}$ as the preferred ion. For everything else, the default settings were used. Resulting peak tables were exported as excel files in three levels of Compounds, Compound per File and Features (just Features for the 'Unaligned') and later saved as csvs. In LipiDex Spectrum Searcher 'LipiDex_HCD_Acetate', 'LipiDex_HCD_Plants', 'LipiDex_Splash_ISTD_Acetate', 'LipiDex_HCD_ULCFA' and 'Ganglioside_20171205' were selected as libraries for the DO while 'LipidBlast2_Reformatted_CoonLab', 'LB_cleaned' and 'Lipid_Spectral_Library_20170523' were selected for the FS. For the cells 'LipiDex_HCD_Acetate', 'LipiDex_HCD_Plants', 'LipiDex_HCD_ULCFA', 'FAHFA' and 'Ganglioside_20200206' were selected. Extended Data Fig. 7 details the lipid classes searched for in these databases with their respective adducts. We further kept the defaults of 0.01-Th for MS1 and MS2 search tolerances, a maximum of one returned search result, and an MS2 low mass cutoff of 61-Th. Under the Peak Finder tab, Compound Discoverer was chosen as peak table type and its 'Aligned' and 'Unaligned' results, as well as the MS/MS results from Spectrum Researcher uploaded. Features had to be identified in a minimum of one file (four files for the FS), however, the average lipid identity was based on a much higher average of 344 features found in plasma and 310 features in the liver dataset. We kept the defaults of a minimum of 75% of lipid spectral purity, an MS2 search dot product of at least 500 and reverse dot product of at least 700, as well as a multiplier of 2.0 (3.0 for FS) for the full width at half-maximum window, a maximum 15 ppm mass difference, adduct/dimer and in-source fragment filtering, and a maximum RT MAD Factor of 3.5. As post-processing all features that were only found in one file and had no identity were deleted and artefactual duplicates deleted.

For the FS liver dataset, peak areas were normalized to the 15:0–18:1(d7)-PC internal standard by dividing each peak area by the internal standards' peak area of that sample and multiplying the result with the median of all internal standard peak areas. The quantification of the internal standard was obtained through TraceFinder v.4.0 (ThermoFisher Scientific). FS plasma results were normalized by dividing each peak area by the feature's average batch control and multiplying with the median feature's peak area over average batch controls. Reported is the $\log_2$ of all normalized values. Note that there are no data available for two CAST females as one animal died before euthanizing (CAST-4) and for another there was not enough plasma (CAST-3). For the cell experiments, peak areas were normalized to the sum of identified lipids and $\log_2$-transformed.

QTL mapping. Of note, while the much smaller FS dataset was normalized to the internal PC standard, for the entire DO dataset, in which many more LC–MS runs were collected, we used a batch correction approach (ComBat) to achieve normalization. In short, the ComBat method provided superior performance, especially in the case of the liver dataset. Specifically, the batch effects that occurred were easily and effectively corrected by application of the ComBat adjustment.

Before mapping analysis, the lipid metabolite data were adjusted for batch effects using the ComBat algorithm[75] as implemented in the R/sva software package[76]. Batches correspond to sets of ~32 samples each that were run on the same day on the mass spectrometer. Effectiveness of batch correction was confirmed by visualization of the first few principal components. We note that batch adjustment substantially increased the yield of QTL, even though no genotype information is used in the correction process.

QTL mapping involves 'scanning' the genome and testing for association between the eight-state haplotype probabilities and the batch corrected MS feature levels. The genome scans were performed for each lipid metabolite feature using the scan1() function in R/qtl2 (ref. [23]). This software fits a linear mixed with sex and DO breeding generation as additive covariates and random effect to account for the kinship structure of the DO mice and computes a $\log_{10}$ likelihood ratio statistic (LOD) to evaluate the significance of the genetic effect at each pseudo-marker locus. Sex-specific genetic associations were identified using a separate set of genome scans that included a sex X genotype interaction in the linear mixed model. We identified suggestive QTL at LOD > 6.0 and notable QTL at LOD > 7.4. These threshold values were estimated by permutation analysis to obtain a family-wise error correction for genome-wide QTL search[68]. The family-wise error rate ensures that the maximum LOD score across the genome-wide search when applied to a trait with no QTL (that is, a permuted trait) will exceed the threshold with a fixed probability. For the lenient threshold 6.0, the genome-wide probability of false QTL detection is 0.20. For the stringent threshold 7.4, the genome-wide error rate is controlled at 0.05. The lenient threshold is used to identify the almost-notable associations that colocalize on the genome in hotspots[77].

Data analysis and plotting. Data analysis was largely performed using R v.3.5.0 (ref. [78]) in RStudio[79]. Data formatting was performed using R/dplyr_0.8.3 (ref. [80]), R/tidyr_1.0.0 (ref. [81]) and R/reshape2_1.4.3 (ref. [82]) and visualizations were created using R/ggplot2_3.2.1 (ref. [83]), R/RColorBrewer_1.1-2 (ref. [84]), and for exploratory analysis, R/plotly_4.9.0 (ref. [85]). Heatmaps were generated using R/pheatmap_1.0.12 (ref. [86]) and Manhattan plots were generated based on code accessible via the R graph gallery[87]. All boxplots were generated by ggplot2:geom_boxplot with the first and third quartiles (25th and 75th percentiles) for lower and upper hinges, 1.5× interquartile range for the length of the whiskers, centre line at median (50% quantile) and all raw data points, including outliers shown. Statistical *t*-test calculations were performed with MetaboAnalyst 4.0 (ref. [88]). A 95% Bayesian confidence interval for each QTL was calculated using the function find_peaks() in R/qtl2.27 Human Mouse homologues were obtained from the MGI homology database (available here: http://www.informatics.jax.org/downloads/reports/HOM_MouseHumanSequence.rpt).

Allele effects for each QTL were generated using the scan1blup() function of R/qtl2 (ref. [27]). SNP associations were performed using the scan1snps() function in R/qtl2_0.20 (ref. [27]) accessing variants from the database cc_variants.sqlite (available here: https://ndownloader.figshare.com/files/18533342) and genes from mouse_genes_mgi.sqlite (available here: https://ndownloader.figshare.com/files/17609252) via R/RSQLite_2.1.2 (ref. [89]).

To nominate candidate gene drivers at lipid-associated QTL, we integrated the lipid data collected in the present study with hepatic gene expression data previously obtained from a separate cohort of DO mice[34]. We reasoned that a locus that demonstrated a hepatic *cis*-eQTL and a lipid-associated QTL with a similar allele effect patterns is likely to be driving the two phenotypes. We focused on *cis*-eQTL, as these are expression traits responding to local genetic variation. We computed the Pearson's correlation between the allele effect patterns for all *cis*-eQTL at a locus to which one or more lipids comapped. We performed the same calculation for hepatic *cis*-pQTL identified in the previous study[34]. For example, at the chromosome 10 locus, we identified >25 QTL of unknown lipids in plasma and liver, all of which showed a strong NOD-driven allele effect pattern. About half of these QTL showed NOD as the high allele and half showed NOD as the low allele. We first computed the average allele effect pattern for the NOD high lipids and the NOD-low lipids. We then identified 55 *cis*-eQTL and 16 *cis*-pQTL that were within ±2 Mbp of the lipid QTL at ~127 Mbp on chromosome 10, and calculated the correlation between their allele effect patterns and the NOD high and NOD-low lipid QTL. One gene showed a very strong correlation: *B4galnt1*. The overall correlation between the allele effects of the lipid QTL and the *cis*-eQTL or *cis*-pQTL was very low (for example, 0), suggesting that most expression traits are responding to genetic variants different from the lipid traits. However, the correlation between the lipid traits and either the expression or protein level for B4galnt1 was >|0.97|. As B4galnt1 is a known gangliosidase, we then asked if the MS fragmentation pattern for the unknown lipids is consistent with gangliosides. It is worth noting that GM3 ganglioside standard (Cayman Chemicals, item no. 15587) contained *N*-acetyl-neuraminidate (NANA), the only sialic acid made by humans. All gangliosides observed in the DO samples contain *N*-glycolyl-neuraminidate (NGNA), a main sialic acid in mice[90,91]. This powerful approach enabled us to combine the lipid data from one DO study with the gene expression and proteomic data of another DO study to nominate one candidate gene.

Reporting Summary. Further information on research design is available in the Nature Research Reporting Summary linked to this article.

Data availability

Genotypes and additional phenotype data associated with the DO mouse population have been deposited with Dryad (https://doi.org/10.5061/dryad.pj105; data files: Attie Islet eQTL data) (see Keller et al., ref. [32], for details). In addition, the data reported here are available for download and interactive web-based analysis at https://churchilllab.jax.org/qtlviewer/attie/islets. Genotyping used the Mouse Universal Genotyping Array (GigaMUGA; 143,259 markers).
MS data have been deposited in Chorus (http://chorusproject.org/) under ID 1610 (direct links to cell experiments https://chorusproject.org/anonymous/download/experiment/4984245205453479277, DO liver https://chorusproject.org/anonymous/download/experiment/a639bcc5602c441c9a1df94f4340d626, DO plasma https://chorusproject.org/anonymous/download/experiment/f8b273d222364f2a9d92cfdd0eb601b6, FS liver https://chorusproject.org/anonymous/download/experiment/c930cd419eb34dfebda7f53508c6969e, and FS plasma https://chorusproject.org/anonymous/download/experiment/9d4d025df0114687924d4075f3c927ca). Human Mouse homologues were obtained from the MGI homology database (available here: http://www.informatics.jax.org/downloads/reports/HOM_MouseHumanSequence.rpt). SNP associations were performed accessing variants from the database cc_variants.sqlite (available here: https://ndownloader.figshare.com/files/18533342) and genes from mouse_genes_mgi.sqlite (available here: https://ndownloader.figshare.com/files/17609252). Figures 1–5 and Extended Data Figs. 1–6 have associated raw data. Source data are provided with this paper.

Code availability

The data preparation and QTL mapping analysis are reproducibly documented in UNIX shell and R scripts posted on github (https://github.com/dmgatti/AttieMetabolomics). Code for data analysis and plotting is available at https://github.com/vanilink/DOLipids/ with input from Supplementary Tables 8 and 9. The genome–lipid associations are also accessible through an interactive web-based

analysis tool that will allow users to replicate the analyses reported here (http://lipidgenie.com/). The source code for this resource can be found at https://github.com/coongroup/LipidGenie.

Received: 3 December 2019; Accepted: 11 August 2020;
Published online: 21 September 2020

References

1. Han, X. Lipidomics for studying metabolism. *Nat. Rev. Endocrinol.* **12**, 668–679 (2016).
2. Yang, L. et al. Recent advances in lipidomics for disease research. *J. Sep. Sci.* **39**, 38–50 (2016).
3. Kind, T. et al. LipidBlast in silico tandem mass spectrometry database for lipid identification. *Nat. Methods* **10**, 755–758 (2013).
4. Gross, R. W. & Han, X. Lipidomics at the interface of structure and function in systems biology. *Chem. Biol.* **18**, 284–291 (2011).
5. Cajka, T. & Fiehn, O. Comprehensive analysis of lipids in biological systems by liquid chromatography-mass spectrometry. *Trends Anal. Chem.* **61**, 192–206 (2014).
6. Tabassum, R. et al. Genetic architecture of human plasma lipidome and its link to cardiovascular disease. *Nat. Commun.* **10**, 4329 (2019).
7. Kiyonami, R., Peake, D. A., Liu, X. & Huang, Y. *Large-scale lipid profiling of a human serum lipidome using a high-resolution, accurate-mass LC/MS/MS approach* Application Note No. 647 (Thermo Fisher Scientific, 2016).
8. Slatter, D. A. et al. Mapping the human platelet lipidome reveals cytosolic phospholipase A2 as a regulator of mitochondrial bioenergetics during activation. *Cell Metab.* **23**, 930–944 (2016).
9. Contrepois, K. et al. Cross-platform comparison of untargeted and targeted lipidomics approaches on aging mouse plasma. *Sci. Rep.* **8**, 17747 (2018).
10. Blaženović, I. et al. Increasing compound identification rates in untargeted lipidomics research with liquid chromatography drift time-ion mobility mass spectrometry. *Anal. Chem.* **90**, 10758–10764 (2018).
11. Mahieu, N. G. & Patti, G. J. Systems-Level annotation of a metabolomics data set reduces 25 000 features to fewer than 1000 unique metabolites. *Anal. Chem.* **89**, 10397–10406 (2017).
12. Blaženović, I., Kind, T., Ji, J. & Fiehn, O. Software tools and approaches for compound identification of LC–MS/MS data in metabolomics. *Metabolites* https://doi.org/10.3390/metabo8020031 (2018).
13. Gross, R. W. The evolution of lipidomics through space and time. *Biochim. Biophys. Acta–Mol. Cell Biol. Lipids* **1862**, 731–739 (2017).
14. Koelmel, J. P. et al. LipidMatch: an automated workflow for rule-based lipid identification using untargeted high-resolution tandem mass spectrometry data. *BMC Bioinf.* **18**, 331 (2017).
15. Hartler, J. et al. Deciphering lipid structures based on platform-independent decision rules. *Nat. Methods* **14**, 1171–1174 (2017).
16. Hutchins, P. D., Russell, J. D. & Coon, J. J. LipiDex: an integrated software package for high-confidence lipid identification. *Cell Syst.* **6**, 621–625.e5 (2018).
17. Hutchins, P. D., Russell, J. D. & Coon, J. J. Mapping lipid fragmentation for tailored mass spectral libraries. *J. Am. Soc. Mass. Spectrom.* **30**, 659–668 (2019).
18. Kostyukevich, Y. et al. Hydrogen/deuterium exchange aiding compound identification for LC–MS and MALDI imaging lipidomics. *Anal. Chem.* **91**, 13465–13474 (2019).
19. Stefely, J. A. et al. Mitochondrial protein functions elucidated by multi-omic mass spectrometry profiling. *Nat. Biotechnol.* **34**, 1191–1197 (2016).
20. Dumas, M.-E. et al. Topological analysis of metabolic networks integrating co-segregating transcriptomes and metabolomes in type 2 diabetic rat congenic series. *Genome Med.* **8**, 101 (2016).
21. Cazier, J.-B. et al. Untargeted metabolome quantitative trait locus mapping associates variation in urine glycerate to mutant glycerate kinase. *J. Proteome Res.* **11**, 631–642 (2012).
22. Krumsiek, J. et al. Mining the unknown: a systems approach to metabolite identification combining genetic and metabolic information. *PLoS Genet.* **8**, e1003005 (2012).
23. Shin, S.-Y. et al. An atlas of genetic influences on human blood metabolites. *Nat. Genet.* **46**, 543–550 (2014).
24. Rueedi, R. et al. Metabomatching: using genetic association to identify metabolites in proton NMR spectroscopy. *PLoS Comput. Biol.* **13**, e1005839 (2017).
25. Raffler, J. et al. Identification and MS-assisted interpretation of genetically influenced NMR signals in human plasma. *Genome Med.* **5**, 13 (2013).
26. Gatti, D. M. et al. Quantitative trait locus mapping methods for diversity outbred mice. *G3* **4**, 1623–1633 (2014).
27. Broman, K. W. et al. R/qtl2: Software for mapping quantitative trait loci with high-dimensional data and multiparent populations. *Genetics* **211**, 495–502 (2019).
28. Svenson, K. L. et al. High-resolution genetic mapping using the mouse diversity outbred population. *Genetics* **190**, 437–447 (2012).
29. Chesler, E. J. et al. Diversity outbred mice at 21: maintaining allelic variation in the face of selection. *G3* **6**, 3893–3902 (2016).
30. Mayer, R. et al. Common themes and cell type specific variations of higher order chromatin arrangements in the mouse. *BMC Cell Biol.* **6**, 44 (2005).
31. Aylor, D. L. et al. Genetic analysis of complex traits in the emerging collaborative cross. *Genome Res.* **21**, 1213–1222 (2011).
32. Keller, M. P. et al. Genetic drivers of pancreatic islet function. *Genetics* **209**, 335–356 (2018).
33. Keller, M. P. et al. Gene loci associated with insulin secretion in islets from nondiabetic mice. *J. Clin. Invest.* **129**, 4419–4432 (2019).
34. Chick, J. M. et al. Defining the consequences of genetic variation on a proteome-wide scale. *Nature* **534**, 500–505 (2016).
35. Kemis, J. H. et al. Genetic determinants of gut microbiota composition and bile acid profiles in mice. *PLoS Genet*. https://doi.org/10.1371/journal.pgen.1008073 (2019).
36. Gallego, S. F., Højlund, K. & Ejsing, C. S. Easy, fast, and reproducible quantification of cholesterol and other lipids in human plasma by combined high resolution MSX and FTMS analysis. *J. Am. Soc. Mass. Spectrom.* **29**, 34–41 (2018).
37. Ogiso, H., Suzuki, T. & Taguchi, R. Development of a reverse-phase liquid chromatography electrospray ionization mass spectrometry method for lipidomics, improving detection of phosphatidic acid and phosphatidylserine. *Anal. Biochem.* **375**, 124–131 (2008).
38. Fahy, E. et al. Update of the LIPID MAPS comprehensive classification system for lipids. *J. Lipid Res.* **50**, S9–S14 (2009).
39. Liebisch, G. et al. Shorthand notation for lipid structures derived from mass spectrometry. *J. Lipid Res.* **54**, 1523–1530 (2013).
40. Su, Z. et al. Genetic basis of HDL variation in 129/SvImJ and C57BL/6J mice: importance of testing candidate genes in targeted mutant mice. *J. Lipid Res.* **50**, 116–125 (2009).
41. Kettunen, J. et al. Genome-wide study for circulating metabolites identifies 62 loci and reveals novel systemic effects of LPA. *Nat. Commun.* **7**, 11122 (2016).
42. Zhang, W. et al. Genome-wide association mapping of quantitative traits in outbred mice. *G3* **2**, 167–174 (2012).
43. Pamir, N. et al. Genetic control of the mouse HDL proteome defines HDL traits, function, and heterogeneity. *J. Lipid Res.* **60**, 594–608 (2019).
44. Wang, X., Korstanje, R., Higgins, D. & Paigen, B. Haplotype analysis in multiple crosses to identify a QTL gene. *Genome Res.* **14**, 1767–1772 (2004).
45. Blanco-Vaca, F., Escolà-Gil, J. C., Martín-Campos, J. M. & Julve, J. Role of apoA-II in lipid metabolism and atherosclerosis: advances in the study of an enigmatic protein. *J. Lipid Res.* **42**, 1727–1739 (2001).
46. Kontush, A., Lhomme, M. & Chapman, M. J. Unraveling the complexities of the HDL lipidome. *J. Lipid Res.* **54**, 2950–2963 (2013).
47. Murphy, R. C., Leiker, T. J. & Barkley, R. M. Glycerolipid and cholesterol ester analyses in biological samples by mass spectrometry. *Biochim. Biophys. Acta* **1811**, 776 (2011).
48. Lerno, L. A. Jr, German, J. B. & Lebrilla, C. B. Method for the identification of lipid classes based on referenced Kendrick mass analysis. *Anal. Chem.* **82**, 4236–4245 (2010).
49. Eilbeck, K. et al. The sequence ontology: a tool for the unification of genome annotations. *Genome Biol.* **6**, R44 (2005).
50. Nagata, Y. et al. Expression cloning of beta 1,4 *N*-acetylgalactosaminyltransferase cDNAs that determine the expression of GM2 and GD2 gangliosides. *J. Biol. Chem.* **267**, 12082–12089 (1992).
51. Dotta, F. et al. Pancreatic islet ganglioside expression in nonobese diabetic mice: comparison with C57BL/10 mice and changes after autoimmune beta-cell destruction. *Endocrinology* **130**, 37–42 (1992).
52. Li, Z. et al. Impact of sphingomyelin synthase 1 deficiency on sphingolipid metabolism and atherosclerosis in mice. *Arterioscler. Thromb. Vasc. Biol.* **32**, 1577–1584 (2012).
53. Bergfeld, A. K. et al. *N*-glycolyl groups of nonhuman chondroitin sulfates survive in ancient fossils. *Proc. Natl Acad. Sci. USA* **114**, E8155–E8164 (2017).
54. Strømme, P. et al. X-linked Angelman-like syndrome caused by Slc9a6 knockout in mice exhibits evidence of endosomal–lysosomal dysfunction. *Brain* **134**, 3369–3383 (2011).
55. Spessott, W., Uliana, A. & Maccioni, H. J. F. Defective GM3 synthesis in Cog2 null mutant CHO cells associates to mislocalization of lactosylceramide sialyltransferase in the golgi complex. *Neurochem. Res.* **35**, 2161–2167 (2010).
56. Ledeen, R. W. & Wu, G. The multi-tasked life of GM1 ganglioside, a true factotum of nature. *Trends Biochem. Sci.* **40**, 407–418 (2015).
57. Yore, M. M. et al. Discovery of a class of endogenous mammalian lipids with anti-diabetic and anti-inflammatory effects. *Cell* **159**, 318–332 (2014).
58. McLean, S., Davies, N. W., Nichols, D. S. & Mcleod, B. J. *Triacylglycerol estolides*, a new class of mammalian lipids, in the paracloacal gland of the brushtail possum (*Trichosurus vulpecula*). *Lipids* **50**, 591–604 (2015).
59. Parker, B. L. et al. An integrative systems genetic analysis of mammalian lipid metabolism. *Nature* **567**, 187–193 (2019).

60. Lord, C. C., Thomas, G. & Brown, J. M. Mammalian alpha beta hydrolase domain (ABHD) proteins: lipid metabolizing enzymes at the interface of cell signaling and energy metabolism. *Biochim. Biophys. Acta* **1831**, 792–802 (2013).
61. Long, J. Z. et al. Metabolomics annotates ABHD3 as a physiologic regulator of medium-chain phospholipids. *Nat. Chem. Biol.* **7**, 763–765 (2011).
62. Draisma, H. H. M. et al. Genome-wide association study identifies novel genetic variants contributing to variation in blood metabolite levels. *Nat. Commun.* **6**, 7208 (2015).
63. Ha, C. Y. et al. The association of specific metabolites of lipid metabolism with markers of oxidative stress, inflammation and arterial stiffness in men with newly diagnosed type 2 diabetes. *Clin. Endocrinol.* **76**, 674–682 (2012).
64. Demirkan, A. et al. Genome-wide association study identifies novel loci associated with circulating phospho- and sphingolipid concentrations. *PLoS Genet.* **8**, e1002490 (2012).
65. Miller, M. R. et al. Unconventional endocannabinoid signaling governs sperm activation via the sex hormone progesterone. *Science* **352**, 555–559 (2016).
66. Baggelaar, M. P., Maccarrone, M. & van der Stelt, M. 2-Arachidonoylglycerol: a signaling lipid with manifold actions in the brain. *Prog. Lipid Res.* **71**, 1–17 (2018).
67. Jha, P. et al. Systems analyses reveal physiological roles and genetic regulators of liver lipid species. *Cell Syst.* **6**, 722–733.e6 (2018).
68. Jha, P. et al. Genetic regulation of plasma lipid species and their association with metabolic phenotypes. *Cell Syst.* **6**, 709–721.e6 (2018).
69. Stacey, D. et al. ProGeM: a framework for the prioritization of candidate causal genes at molecular quantitative trait loci. *Nucleic Acids Res.* **47**, e3 (2019).
70. Kastenmüller, G., Raffler, J., Gieger, C. & Suhre, K. Genetics of human metabolism: an update. *Hum. Mol. Genet.* **24**, R93–R101 (2015).
71. Mitok, K. A. et al. Islet proteomics reveals genetic variation in dopamine production resulting in altered insulin secretion. *J. Biol. Chem.* **293**, 5860–5877 (2018).
72. Broman, K. W., Gatti, D. M., Svenson, K. L., Sen, Ś. & Churchill, G. A. Cleaning genotype data from diversity outbred mice. *G3* **9**, 1571–1579 (2019).
73. Choi, K. B. churchill-lab/gbrs v.0.1.5 (Zenodo, 2017); https://doi.org/10.5281/zenodo.291787
74. Adusumilli, R. & Mallick, P. Data conversion with ProteoWizard msConvert. *Methods Mol. Biol.* **1550**, 339–368 (2017).
75. Johnson, W. E., Evan Johnson, W., Li, C. & Rabinovic, A. Adjusting batch effects in microarray expression data using empirical Bayes methods. *Biostatistics* **8**, 118–127 (2007).
76. Leek, J. T., Johnson, W. E., Parker, H. S., Jaffe, A. E. & Storey, J. D. The sva package for removing batch effects and other unwanted variation in high-throughput experiments. *Bioinformatics* **28**, 882–883 (2012).
77. Churchill, G. A. & Doerge, R. W. Empirical threshold values for quantitative trait mapping. *Genetics* **138**, 963–971 (1994).
78. R Core Team. *R: A Language and Environment for Statistical Computing* (R Foundation for Statistical Computing, 2019).
79. RStudio Team. *RStudio: Integrated Development Environment for R* (RStudio, 2016).
80. Wickham, H., François, R., Henry, L. & Müller, K. dplyr: A grammar of data manipulation (2019).
81. Wickham, H. & Henry, L. tidyr: Tidy messy data (2019).
82. Wickham, H. et al. Reshaping data with the reshape package. *J. Stat. Softw.* **21**, 1–20 (2007).
83. Wickham, H. *ggplot2: Elegant Graphics for Data Analysis* (Springer, 2016).
84. Neuwirth, E. RColorBrewer: ColorBrewer palettes (2014).
85. Sievert, C. plotly for R (2018).
86. Kolde, R. pheatmap: Pretty heatmaps (2019).
87. Holtz, Y. Manhattan plot in R: a review. *R graph gallery* https://www.r-graph-gallery.com/101_Manhattan_plot.html (2019).
88. Chong, J. et al. MetaboAnalyst 4.0: towards more transparent and integrative metabolomics analysis. *Nucleic Acids Res.* **46**, W486–W494 (2018).
89. Müller, K., Wickham, H., James, D. A. & Falcon, S. RSQLite: 'SQLite' interface for R (2019).
90. Kavaler, S. et al. Pancreatic beta-cell failure in obese mice with human-like CMP-Neu5Ac hydroxylase deficiency. *FASEB J.* **25**, 1887–1893 (2011).
91. Salama, A. et al. Neu5Gc and α1-3 GAL xenoantigen knockout does not affect glycemia homeostasis and insulin secretion in pigs. *Diabetes* **66**, 987–993 (2017).
92. Matyash, V., Liebisch, G., Kurzchalia, T. V., Shevchenko, A. & Schwudke, D. Lipid extraction by methyl-*tert*-butyl ether for high-throughput lipidomics. *J. Lipid Res.* **49**, 1137–1146 (2008).

Acknowledgements

This work was supported by National Institutes of Health grant nos. P41 GM108538 and 2R01DK101573. This research was performed using the compute resources and assistance of the UW–Madison Center For High Throughput Computing (CHTC) in the Department of Computer Sciences. The CHTC is supported by UW–Madison, the Advanced Computing Initiative, the Wisconsin Alumni Research Foundation, the Wisconsin Institutes for Discovery, and the National Science Foundation, and is an active member of the Open Science Grid, which is supported by the National Science Foundation and the US Department of Energy's Office of Science. We thank B. Paulson for help with sample preparation and D. Hwang for help with figures. We thank J. Simcox (Department of Biochemistry, University of Wisconsin–Madison, Madison) for providing the His-tagged CMV6-GFP plasmid and Hepa1-6 cells.

Author contributions

J.D.R., M.P.K., G.A.C., A.D.A. and J.J.C. designed the experiment. K.L.S., D.S.S., M.E.R. and M.P.K. assisted with sample collection. V.L., P.D.H., E.A.T. and T.R.R. performed the MS analysis. E.M.C. performed cell experiments. V.L., I.J.M., D.R.B., P.D.H., M.P.K., D.M.G., G.R.K., D.P. and G.A.C. analysed data. V.L., K.A.O., I.J.M., M.P.K., K.W.B., G.A.C., A.D.A. and J.J.C. wrote the manuscript.

Competing interests

The authors declare no competing interests.

Additional information

Extended data is available for this paper at https://doi.org/10.1038/s42255-020-00278-3.

Supplementary information is available for this paper at https://doi.org/10.1038/s42255-020-00278-3.

Correspondence and requests for materials should be addressed to J.J.C.

Peer review information Primary Handling Editor: Pooja Jha.

Reprints and permissions information is available at www.nature.com/reprints.

Publisher's note Springer Nature remains neutral with regard to jurisdictional claims in published maps and institutional affiliations.

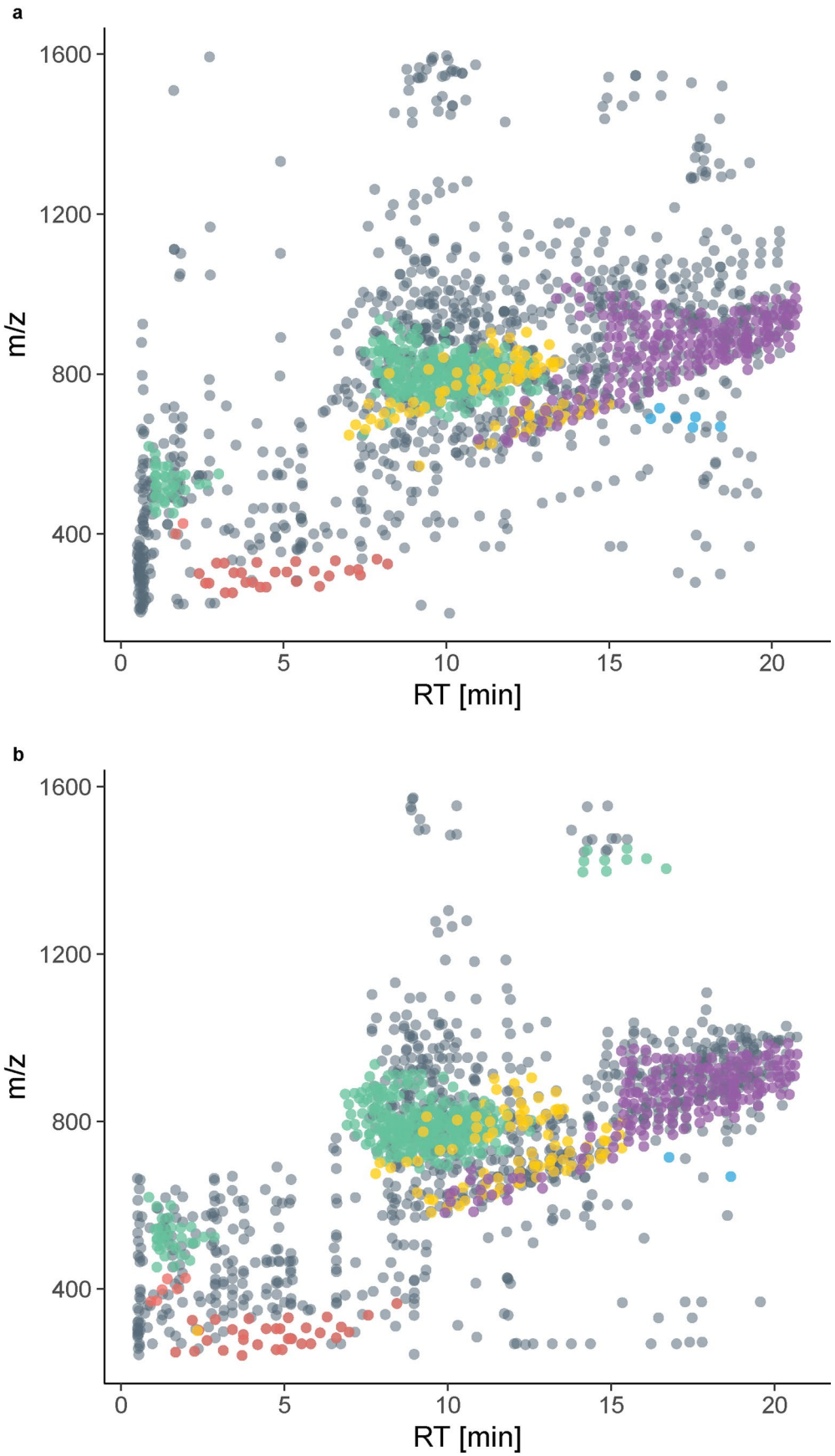

Extended Data Fig. 1 | Identified lipids and unidentified features occupy characteristic regions in the m/z vs. RT space. a, In plasma, we quantified 1,721 lipidomic features, 621 of which were identified, and **b**, In liver, we quantified 1,562 lipidomic features, 615 of which were identified. Abbreviations: m/z (mass-to-charge), RT (retention time).

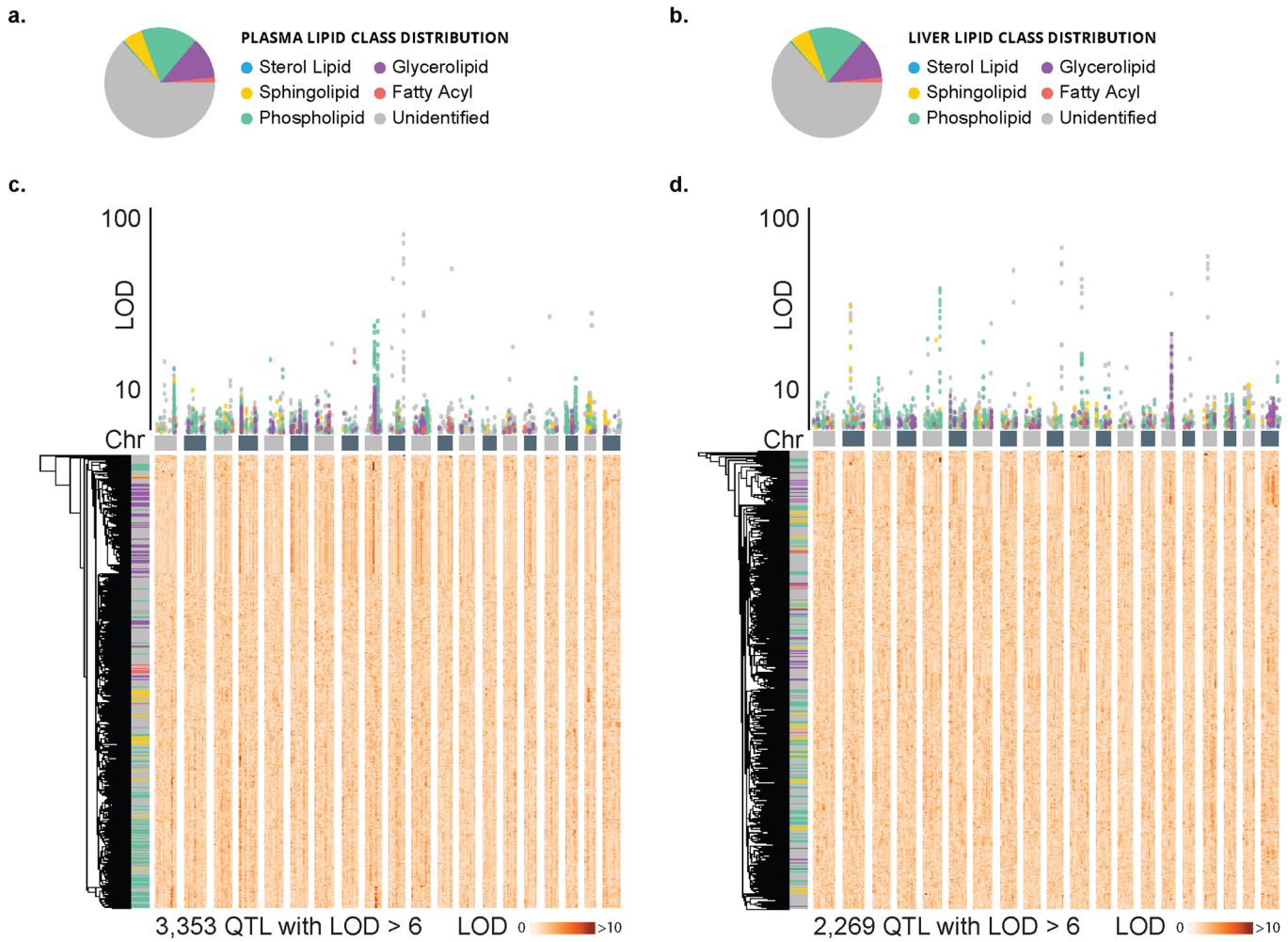

Extended Data Fig. 2 | Lipid profiling and subsequent QTL mapping reveals clusters of associated lipids. a, Lipid class distribution of all 1,721 plasma and **b**, 1,562 liver lipidomic features. **c**, 1,405 plasma and **d**, 1,190 lipid features showed at least one QTL with an LOD > 6 as displayed in a Manhattan plot (n = 3,353 and 2,269 total QTL, respectively). Hierarchical clustering of these features against the 69,005 markers on the mouse genome, resulted in clustering of lipid class based on hotspots at the genetic level. Abbreviations: Chr (chromosome), DO (diversity outbred), QTL (quantitative trait loci), LOD (logarithm of odds).

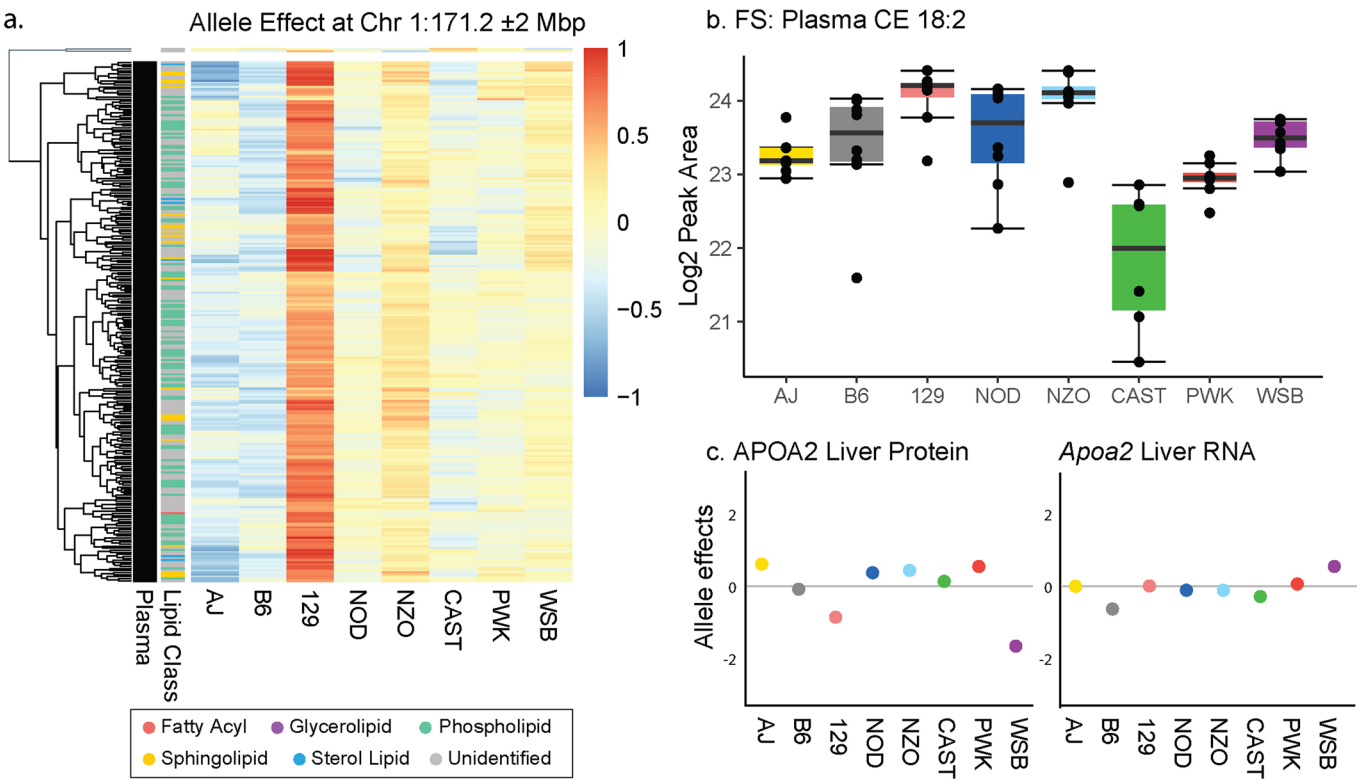

Extended Data Fig. 3 | *Apoa2* as the candidate gene at the largest lipid hotspot. a, 255 plasma (black) features mapping to the apoa2 locus on chromosome 1 share an allele effect pattern with upregulation in the 129 allele, while 2 mapping liver features (white) do not share the pattern (based on hierarchical clustering on allele effects, with a Euclidean distance cutoff of h = 1.5). **b**, The allele effect is exemplary replicated in an independent experiment of founder strain plasma CE(18:2) levels (n = 4 for each sex and strain, boxplots are defined with the first and third quartiles (25th and 75th percentile) for lower and upper hinges, 1.5x interquartile range for the length of the whiskers, centre line at median (50% quantile)). **c**, The same pattern was not visible in previously reported[34] Apoa2 liver protein and RNA allele effects. Abbreviations: CE (cholesteryl ester), FS (founder strain).

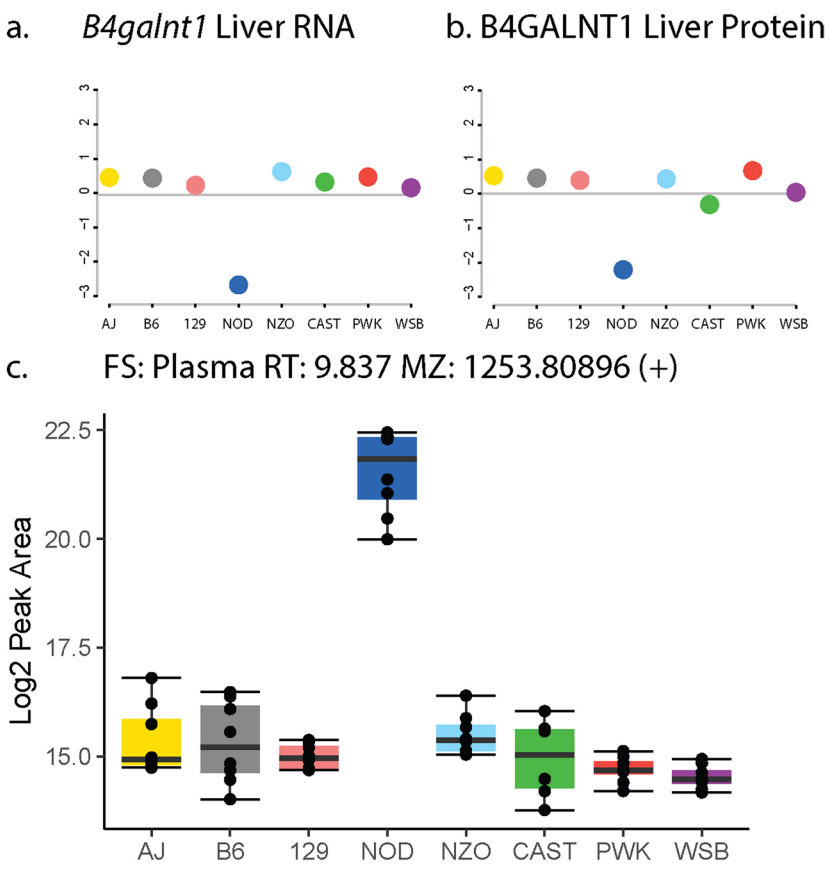

Extended Data Fig. 4 | *B4galnt1* as the candidate gene at the hotspot with the largest LOD. a, The selection of *B4galnt1* as the candidate gene for the chromosome 10:127 Mbp locus was corroborated by NOD-specific allele effects in previously reported liver eQTL and **b**, pQTL[34]. c, The allele effect patterns of the later as gangliosides identified features mapping to the *B4galnt1* locus could further be validated in an independent experiment of founder strain mice (exemplar GM3 pattern, n = 4 for each sex and strain, boxplots are defined with the first and third quartiles (25th and 75th percentile) for lower and upper hinges, 1.5x interquartile range for the length of the whiskers, center line at median (50% quantile)). Abbreviations: FS (founder strain), Mbp (megabase pair).

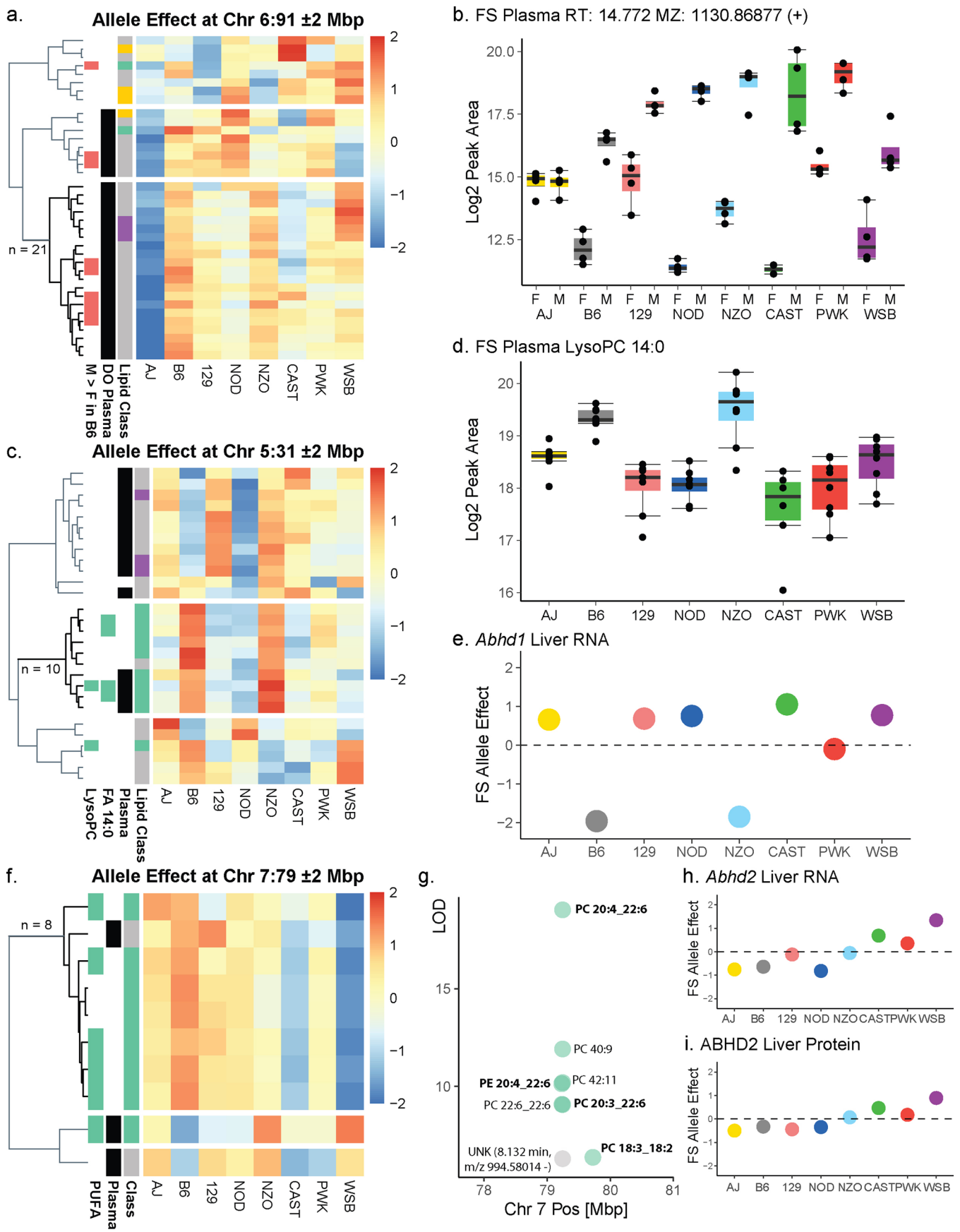

Extended Data Fig. 5 | See next page for caption.

Extended Data Fig. 5 | Allele effects characterize genome-lipid hotspots. a, Hierarchical clustering of allele effects at Chr 6:91 Mbp resulted in 21 features with matching A/J down effect (main cluster featuring the six B6 male specific features (red) after row-scaling and Ward clustering, cutoff at h=5). **b**, Consistently, the pattern of male >> female was observed for each of the FS except for A/J as visible in the example for *m/z* 1130 (n = 4 for each sex and strain, boxplots are defined with the first and third quartiles (25th and 75th percentile) for lower and upper hinges, 1.5x interquartile range for the length of the whiskers, center line at median (50% quantile).) **c**, Hierarchical clustering of allele effects at Chr 5:31 Mbp locus resulted in 10 features with matching B6 and NZO up effect (main cluster featuring LysoPC 14:0 (turquoise) after row-scaling and Ward clustering, cutoff at h=8). **d**, This pattern could be replicated in the FS (n = 4 for each sex and strain, boxplots are defined with the first and third quartiles (25th and 75th percentile) for lower and upper hinges, 1.5x interquartile range for the length of the whiskers, center line at median (50% quantile)), as shown for LysoPC 14:0, as well as **e**, in opposite directionality in a liver eQTL[34]. **f**, Hierarchical clustering of allele effects at Chr 7:79 Mbp locus resulted in 8 features with matching WSB down effect (main cluster featuring PUFA-containing phospholipids (turquoise) after row-scaling and Ward clustering, cutoff at h=2.5). **g**, The mapping phospholipids contained polyunsaturated fatty acids such as 20:4 and 22:6. **h**-**i**, *Abhd2* liver RNA and protein allele effects[34] matched with an opposite WSB high effect. Abbreviations: DO (diversity outbred), FS (founder strain), Chr (chromosome), Mbp (megabase pair), PC (phosphatidylcholine), PUFA (polyunsaturated fatty acid).

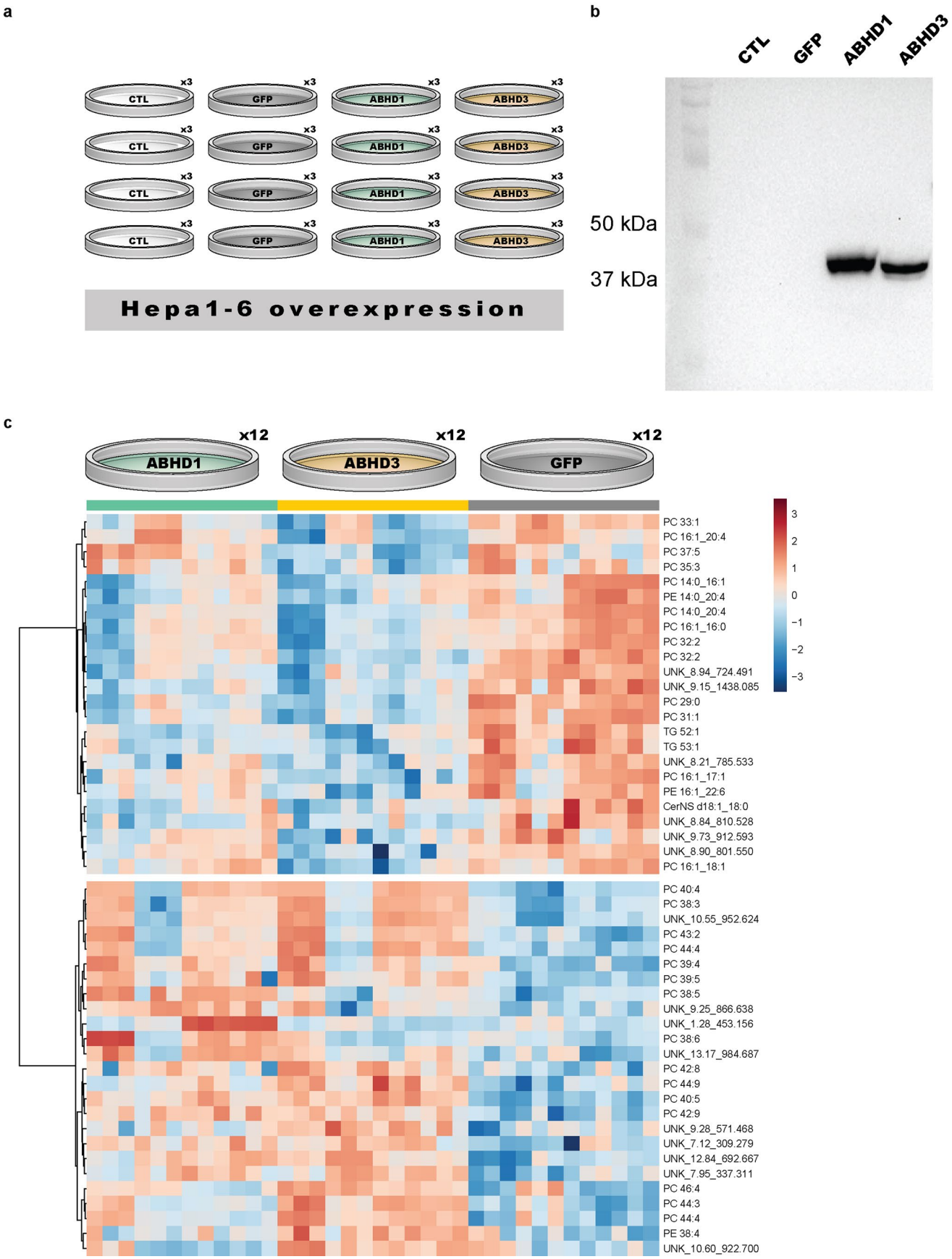

Extended Data Fig. 6 | See next page for caption.

Extended Data Fig. 6 | Overexpressing ABHD1 and ABHD3 results in distinct phospholipid signature. a, Experimental design of the validation experiment featuring three technical and four biological replicates of Hepa1-6 cells either untransfected (CTL), transfected with a His-tag GFP control (GFP), or transfected with MYC-tagged ABHD1 or ABHD3. **b**, Western blot of Hepa1-6 overexpression of ABHD1 and ABHD3. Shown is an overlay of membrane and ECL blot for MYC-tag. **c**, Heatmap of top 49 features from discovery lipidomics experiment with $p < 0.05$ (ANOVA, Fisher's LSD post-hoc). Features were sum-normalized and log2-transformed. Hierarchical clustering (Ward clustering, Euclidean distance) shows two clusters with opposite fold changes distinguishing between ABHD1 and ABHD3 and the GFP control.

Abbreviation	Lipid Class	Adduct(s)
AC	Acyl Carnitine	[M+H]+
Alkanyl-TG	Alkanyl Triacylglycerol	[M+NH4]+
Alkenyl-TG	Alkenyl Triacylglycerol	[M+NH4]+
Alkenyl-DG	Alkenyl Diacylglycerol	[M+H]+
CE	Cholesteryl ester	[M+NH4]+
Cer [AP]	CeramideAP	[M-H]-; [M+Ac-H]-
Cer [AS]	CeramideAS	[M+Ac-H]-; [M-H]-
Cer [BS]	CeramideBS	[M-H]-; [M+Ac-H]-
Cer [NP]	CeramideNP	[M-H]-; [M+Ac-H]-
Cer [NS]	CeramideNS	[M+H]+; [M+Ac-H]-; [M-H]-; [M+H-H2O]+
CerP	Ceramide-1-Phosphate	[M+H]+; [M-H]-
CL	Cardiolipin	[M-H]-; [M-2H]2-
DG	Diacylglycerol	[M+NH4]+
DGDG	Dihexosyldiacylglycerol	[M+H]+; [M-H]-; [M+Ac-H]-
FA	Fatty acid	[M-H]-
GD2-NGNA	GD2-Ganglioside-N-Glycolylneuraminic acid	[M+H]+
GD3-NGNA	GD3-Ganglioside-N-Glycolylneuraminic acid	[M+H]+
GM1-NGNA	GM1-Ganglioside-N-Glycolylneuraminic acid	[M+H]+
GM2-NANA	GM2-Ganglioside-N-Acetylneuraminic acid	[M+H]+
GM2-NGNA	GM2-Ganglioside-N-Glycolylneuraminic acid	[M+H]+
GM3-NANA	GM3-Ganglioside-N-Acetylneuraminic acid	[M+H]+
GM3-NGNA	GM3-Ganglioside-N-Glycolylneuraminic acid	[M+H]+
HexCer [AP]	Hexosyl CeramideAP	[M+Ac-H]-
HexCer [NS]	Hexosyl CeramideNS	[M+H]+; [M-H]-; [M+Ac-H]-
LysoPC	Lysophosphatidylcholine	[M+H]+; [M+Ac-H]-
LysoPE	Lysophosphatidylethanolamine	[M+H]+; [M-H]-
LysoPG	Lysophosphatidylglycerol	[M-H]-
LysoPI	Lysophosphatidylinositol	[M-H]-
LysoPS	Lysophosphatidyl serine	[M-H]-
LysoSM	Lysosphingomyelin	[M+H]+; [M+Ac-H]-
Methyl-PA	Methylphosphatidic Acid	[M-H]-
MGDG	Monohexosyldiacylglycerol	[M+NH4]+; [M+Ac-H]-
PA	Phosphatidic acid	[M+NH4]+; [M-H]-
PC	Phosphatidylcholine	[M+H]+; [M+Ac-H]-
PE	Phosphatidylethanolamine	[M+H]+; [M-H]-
PE-NMe	Monomethyl Phosphatidylethanolamine	[M+H]+; [M-H]-
PE-NMe2	Dimethyl Phosphatidylethanolamine	[M+H]+; [M-H]-
PG	Phosphatidylglycerol	[M+NH4]+; [M-H]-
PI	Phosphatidylinositol	[M-H]-; [M+NH4]+; [M+H]+
Plasmanyl-PC	Plasmanyl Phosphatidycholine	[M+H]+; [M+Ac-H]-
Plasmanyl-PE	Plasmanyl Phosphatidylethanolamine	[M-H]-
Plasmenyl-PC	Plasmenylphosphatidylcholine	[M+H]+; [M+Ac-H]-
Plasmenyl-PE	Plasmenylphosphatidylethanolamine	[M+H]+; [M-H]-
PS	Phosphatidylserine	[M+H]+; [M-H]-
S1P	Sphingosine-1-Phosphate	[M+H]+; [M-H]-
SHexCer	Sulfatides	[M+H]+; [M-H]-
SM	Sphingomyelin	[M+H]+; [M+Ac-H]-
SP	Sphingosine	[M+H]+; [M+H-H2O]+
SQDG	Sulfoquinovosyldiacylglycerol	[M+NH4]+; [M-H]-
TG	Triacylglycerol	[M+NH4]+; [M+Na]+

Extended Data Fig. 7 | Lipid class abbreviations and identifications with respective adduct types. As searched for in LipiDex databases (see Methods).

nature research

Corresponding author(s): Coon, Joshua J.

Last updated by author(s): Jul 19, 2020

Reporting Summary

Nature Research wishes to improve the reproducibility of the work that we publish. This form provides structure for consistency and transparency in reporting. For further information on Nature Research policies, see our Editorial Policies and the Editorial Policy Checklist.

Statistics

For all statistical analyses, confirm that the following items are present in the figure legend, table legend, main text, or Methods section.

n/a	Confirmed	
☐	☒	The exact sample size (*n*) for each experimental group/condition, given as a discrete number and unit of measurement
☐	☒	A statement on whether measurements were taken from distinct samples or whether the same sample was measured repeatedly
☐	☒	The statistical test(s) used AND whether they are one- or two-sided *Only common tests should be described solely by name; describe more complex techniques in the Methods section.*
☐	☒	A description of all covariates tested
☐	☒	A description of any assumptions or corrections, such as tests of normality and adjustment for multiple comparisons
☐	☒	A full description of the statistical parameters including central tendency (e.g. means) or other basic estimates (e.g. regression coefficient) AND variation (e.g. standard deviation) or associated estimates of uncertainty (e.g. confidence intervals)
☐	☒	For null hypothesis testing, the test statistic (e.g. *F*, *t*, *r*) with confidence intervals, effect sizes, degrees of freedom and *P* value noted *Give P values as exact values whenever suitable.*
☐	☒	For Bayesian analysis, information on the choice of priors and Markov chain Monte Carlo settings
☒	☐	For hierarchical and complex designs, identification of the appropriate level for tests and full reporting of outcomes
☐	☒	Estimates of effect sizes (e.g. Cohen's *d*, Pearson's *r*), indicating how they were calculated

Our web collection on statistics for biologists contains articles on many of the points above.

Software and code

Policy information about availability of computer code

Data collection

Plasma. Ten microliters of lipid extract were injected through SII for Xcalibur by an Ultimate 3000 RSLC autosampler (Thermo Scientific) coupled to a Q Exactive Focus mass spectrometer run by Tune software version 2.5.0.2042 (Thermo Scientific).
Liver. One microliter of lipid extract was injected through SII for Xcalibur (Thermo Scientific) by a Vanquish Split Sampler HT autosampler (Thermo Scientific) coupled to a Q Exactive HF mass spectrometer run by Tune software version 2.8.0.2688 (Thermo Scientific).
Cells. Ten microliters of lipid extract were injected through SII for Xcalibur (Thermo Scientific) by a Vanquish Split Sampler HT autosampler (Thermo Scientific) coupled to a Q Exactive HF mass spectrometer run by Tune software version 2.9.3.2948 (Thermo Scientific).

Data analysis

The resulting LC-MS lipidomics raw files were converted to mgf files via MSConvertGUI (ProteoWizard, Dr. Parag Mallick, Stanford University) and processed using Compound Discoverer 2.0 (Thermo Fisher Scientific) and an in-house developed open-source software suite, LipiDex. The quantification of the internal standard was obtained through TraceFinder 4.0 (Thermo Fisher Scientific).
Data analysis was largely performed using R in RStudio. The lipid metabolite data were adjusted for batch effects using the Combat algorithm as implemented in the R/sva software package. The genome scans were performed using the scan1() function in R/qtl2. Data formatting was performed utilizing R/dplyr_0.8.3, R/tidyr_1.0.0 and R/reshape2_1.4.3 and visualizations were created using R/ggplot2_3.2.1, R/RColorBrewer_1.1-2, and for exploratory analysis, R/plotly_4.9.0. Heatmaps were generated using R/pheatmap_1.0.12 and manhattan plots were generated based on code accessible via the R graph gallery. All boxplots were generated by ggplot2:geom_boxplot. A 95% Bayesian confidence interval (CI) for each QTL was calculated using the function find_peaks() in R/qtl2. Allele effects for each QTL were generated using the scan1blup() function of R/qtl2. SNP associations were performed using the scan1snps() function in R/qtl2_0.20 accessing variants from the database cc_variants.sqlite (available here: https://ndownloader.figshare.com/files/18533342) and genes from mouse_genes_mgi.sqlite (available here: https://ndownloader.figshare.com/files/17609252) via R/RSQLite_2.1.2.
The data preparation and QTL mapping analysis are reproducibly documented in UNIX shell and R scripts posted on github (https://github.com/dmgatti/AttieMetabolomics). Code for data analysis and plotting is available at https://github.com/vanilink/DOLipids/ with input from Supplementary Tables S8 and S9. The genome-lipid associations are also accessible through an interactive web-based analysis tool that will allow users to replicate the analyses reported here (http://lipidgenie.com/). The source code for this resource can be found at https://

github.com/coongroup/LipidGenie.

For manuscripts utilizing custom algorithms or software that are central to the research but not yet described in published literature, software must be made available to editors and reviewers. We strongly encourage code deposition in a community repository (e.g. GitHub). See the Nature Research guidelines for submitting code & software for further information.

Data

Policy information about availability of data

All manuscripts must include a data availability statement. This statement should provide the following information, where applicable:

- Accession codes, unique identifiers, or web links for publicly available datasets
- A list of figures that have associated raw data
- A description of any restrictions on data availability

Genotypes and additional phenotype data associated with the DO mouse population have been deposited with Dryad (doi:10.5061/dryad.pj105; data files: Attie Islet eQTL data). In addition, the data reported here are available for download and interactive web-based analysis at https://churchilllab.jax.org/qtlviewer/attie/islets. Genotyping used the Mouse Universal Genotyping Array (GigaMUGA; 143,259 markers).
Mass spectrometry data have been deposited in Chorus (http://chorusproject.org/) under ID 1610 (direct links to cell experiments https://chorusproject.org/anonymous/download/experiment/4984245205453479277, DO liver https://chorusproject.org/anonymous/download/experiment/a639bcc5602c441c9a1df94f4340d626, DO plasma https://chorusproject.org/anonymous/download/experiment/f8b273d222364f2a9d92cfdd0eb601b6, FS liver https://chorusproject.org/anonymous/download/experiment/c930cd419eb34dfebda7f53508c6969e, and FS plasma https://chorusproject.org/anonymous/download/experiment/9d4d025df0114687924d4075f3c927ca).
Human Mouse homologues were obtained from the MGI homology database (available here: http://www.informatics.jax.org/downloads/reports/HOM_MouseHumanSequence.rpt). SNP associations were performed accessing variants from the database cc_variants.sqlite (available here: https://ndownloader.figshare.com/files/18533342) and genes from mouse_genes_mgi.sqlite (available here: https://ndownloader.figshare.com/files/17609252).

Field-specific reporting

Please select the one below that is the best fit for your research. If you are not sure, read the appropriate sections before making your selection.

☒ Life sciences ☐ Behavioural & social sciences ☐ Ecological, evolutionary & environmental sciences

For a reference copy of the document with all sections, see nature.com/documents/nr-reporting-summary-flat.pdf

Life sciences study design

All studies must disclose on these points even when the disclosure is negative.

Sample size	A sample size of four waves of 100 mice was chosen. A total of n=384 mice were sacrificed at ~22 weeks of age. This cohort of mice analyzed for this study existed and was previously described.[32, 33, 72] 32. Keller, M. P. et al. Genetic Drivers of Pancreatic Islet Function. Genetics 209, 335–356 (2018). 33. Keller, M. P. et al. Gene loci associated with insulin secretion in islets from nondiabetic mice. Journal of Clinical Investigation vol. 129 4419–4432 (2019). 72. Mitok, K. A. et al. Islet proteomics reveals genetic variation in dopamine production resulting in altered insulin secretion. Journal of Biological Chemistry vol. 293 5860–5877 (2018). For the cell validation experiments, a sample size of n=12 was chosen (n=3 biological replicates x n=4 technical replicates) for each mutant and control based on previous experience with the minimum samples size required for MS validation experiments. Sample size calculation was not performed, but deemed sufficient for the purpose upon observing statistical significance in data analysis.
Data exclusions	No data were excluded from the analyses.
Replication	"Although there is no biological replication of genetically identical animals in an outcross population, there is replication of genotypes at specific loci. This local genetic replication enables one to link phenotype with genotype, as in a human GWAS or QTL mapping studies in DO mice."[32] 32. Keller, M. P. et al. Genetic Drivers of Pancreatic Islet Function. Genetics 209, 335–356 (2018). In addition, the founder strain (FS) data set represents a way of confirming or supporting the gene-lipid associations found in the DO. Several of such instances are highlighted in the manuscript, while the full FS data set is provided in the supplement to enable others to use the founder strain data for additional examples not discussed in the manuscript. As noted above, cell validation experiments were performed in biological and technical replicate. For all MS experiments, subsets of samples were re-analyzed as technical replicates on the LC-MS platform and the results successfully reproduced (i.e. analysis reproducibility).
Randomization	Mice were allocated by waves of 100 each with an equal number of males and females. Samples were randomized into batches for sample preparation and randomized again for running on the LC-MS system. Cell samples were also randomized for sample preparation and randomized again for running on the LC-MS system.
Blinding	Blinding was not relevant to this study as there were no groups.

Reporting for specific materials, systems and methods

We require information from authors about some types of materials, experimental systems and methods used in many studies. Here, indicate whether each material, system or method listed is relevant to your study. If you are not sure if a list item applies to your research, read the appropriate section before selecting a response.

Materials & experimental systems

n/a	Involved in the study
☐	☒ Antibodies
☐	☒ Eukaryotic cell lines
☒	☐ Palaeontology and archaeology
☐	☒ Animals and other organisms
☒	☐ Human research participants
☒	☐ Clinical data
☒	☐ Dual use research of concern

Methods

n/a	Involved in the study
☒	☐ ChIP-seq
☒	☐ Flow cytometry
☒	☐ MRI-based neuroimaging

Antibodies

Antibodies used

Rabbit anti-MYC antibody, CST, 2278 clone 71D10, lot: 5
Goat anti-rabbit-HRP conjugated antibody, CST, 7074S, lot: 24

Validation

The company validated the antibody and expects reactivity against all species since the tag is a humanized MYC that would not otherwise be present in our Hepa1-6 cells. In-house, we further validated by running untransfected control cells, and cells transferred with an untagged control plasmid (GFP) as comparison.

"Myc-tag (71D10) Rabbit mAb detects recombinant proteins containing the Myc epitope tag. The antibody recognizes the Myc-tag fused to either the amino acid or carboxy terminus of targeted proteins in transfected cells. During the production process, side by side comparisons are performed between the new antibody lot and the previous lot. New lots are not released for sale unless the performance is equal to or better than the previous lot in each application. In our tests of the #2278 antibody, we were able to detect Myc-Akt in our transfected cell lines. No signal was observed in the non-transfected controls.

The Myc epitope tag is widely used to detect expression of recombinant proteins in bacteria, yeast, insect and mammalian cell systems. [Munro, S. and Pelham, H.R. (1984) EMBO J 3, 3087-93.]"
See manufacturer's note here: https://www.cellsignal.com/products/primary-antibodies/myc-tag-71d10-rabbit-mab/2278

Eukaryotic cell lines

Policy information about cell lines

Cell line source(s)

Hepa1-6 cells (ATCC® CRL-1830)

Authentication

We did not authenticate in-house. Cells were purchased directly from ATCC by J. Simcox, and propagated for use in our lab.

Mycoplasma contamination

We did save scraped cell RNA to test for mycoplasma but could not run the qPCR due to the lab shutdown.

Commonly misidentified lines
(See ICLAC register)

No commonly misidentified cell lines were used in this study.

Animals and other organisms

Policy information about studies involving animals; ARRIVE guidelines recommended for reporting animal research

Laboratory animals

Equal numbers of male and female Diversity Outbred (DO) mice and the eight founder strains (C57BL/6J (B6), A/J, 129S1/SvImJ (129), NOD/ShiLtJ (NOD), NZO/HILtJ (NZO), PWK/PhJ (PWK), WSB/EiJ (WSB), and CAST/EiJ (CAST)) were all obtained from the Jackson Labs and have been previously described.[32,33,72] Briefly, all mice were housed within the vivarium at the Biochemistry Department, University of Wisconsin-Madison, and maintained on a Western-style high-fat/high-sucrose (HF/HS) diet (44.6% kcal fat, 34% carbohydrate and 17.3% protein) from Envigo Teklad (TD.08811) for 16 weeks. All mice were maintained in a temperature and humidity-controlled room on a 12 hr light/dark cycle (lights on at 6AM and off at 6PM), and provided water ad libitum. At ~22 weeks of age, mice were sacrificed following a 4 hr fast.

32. Keller, M. P. et al. Genetic Drivers of Pancreatic Islet Function. Genetics 209, 335–356 (2018).
33. Keller, M. P. et al. Gene loci associated with insulin secretion in islets from nondiabetic mice. Journal of Clinical Investigation vol. 129 4419–4432 (2019).
72. Mitok, K. A. et al. Islet proteomics reveals genetic variation in dopamine production resulting in altered insulin secretion. Journal of Biological Chemistry vol. 293 5860–5877 (2018).

Wild animals

The study did not involve wild animals.

Field-collected samples	The study did not involve samples collected from the field.
Ethics oversight	All experiments involving mice were preapproved by an AAALAC-accredited institutional Animal Care and Use Committee of the College of Agriculture and Life Sciences (CALS) at the University of Wisconsin-Madison. The CALS Animal Care and Use Protocol number associated with the study is A005821, A. D. Attie, Principal Investigator.

Note that full information on the approval of the study protocol must also be provided in the manuscript.